

**Investigations on the Photocatalytic  
Properties of Novel Layered *Sillen-Aurivillius*  
Perovskite Phases**

**Kaustav Chatterjee**

**MP15012**

*A dissertation submitted for the partial fulfilment of*

*MS degree in Science*



**Department of Chemical Sciences  
Indian Institute of Science Education and Research Mohali  
April 2018**



*Dedicated to my grandparents and Mashimoni*

*for their love and affection...*



## CERTIFICATE OF EXAMINATION

This is to certify that the dissertation titled “**Investigations on the Photocatalytic Properties of Novel Layered *Sillen-Aurivillius* Perovskite Phases**” submitted by Mr. Kaustav Chatterjee (Reg. No. MP15012) for the partial fulfilment of MS degree programme of the Institute, has been examined by the thesis committee duly appointed by the Institute. The committee finds the work done by the candidate satisfactory and recommends that the report be accepted.

Dr. R.Vijaya Anand

Dr. Sugumar Venkataramani

Dr. Ujjal K. Gautam

(Supervisor)



## DECLARATION

The work presented in this dissertation has been carried out by me under the guidance of **Dr. Ujjal K. Gautam** at the Department of Chemical Sciences, Indian Institute of Science Education and Research Mohali.

This work has not been submitted in part or in full for a degree, a diploma, or a fellowship to any other university or institute. Whenever contributions of others are involved, every effort is made to indicate this clearly, with due acknowledgement of collaborative research and discussions. This thesis is a bonafide record of original work done by me and all sources listed within have been detailed in the bibliography.

**Kaustav Chatterjee**  
**MP15012**

Date:  
Place:

In my capacity as the supervisor of the candidate's project work, I certify that the above statements by the candidate are true to the best of my knowledge.

**Dr. Ujjal K. Gautam**  
(Supervisor)

Date:  
Place:





## ACKNOWLEDGEMENT

First and foremost, I wish to thank my advisor, *Dr. Ujjal K. Gautam*, (Department of Chemical Sciences, IISERM). It has been an honour to carry out my MS thesis under his able guidance. I still remember the first words he said to me, “I am true to the word ‘Guide’, and I am no more your teacher!” He has taught me, both consciously and unconsciously, how science is done. I cherish all the brain storming sessions, ideas, criticism and moral support he had offered to make the experience productive and stimulating. The joy and enthusiasm he has for science was motivational for me, even during tough times. I would also take the opportunity to thank him for shaping me as an individual to think independently.

I express my sincere thanks to *Prof. Debi Prasad Sarkar* (Director, IISERM), *Prof. N. Sathyamurthy* (Former Director, IISERM), *Dr. S.Arulananda Babu* (Head, Dept. of Chemical Sciences, IISERM) and *Prof. K. S. Viswanathan* (Former Head, Dept. of Chemical Sciences, IISERM) for providing excellent research facilities in IISER, Mohali. I would like to thank my committee members *Dr. R.Vijaya Anand* and *Dr. Sugumar Venkataramani* for their help and encouragement.

My sincere thanks to all the members of NEL, *Dr.Karthik*, *Dr.Moumita*, *Dr.Arabinda*, *Sanjit*, *Lipipuspa*, *Bhati*, *Neeru*, *Masuma*, *Reeya* for their unconditional support, and I have gained a lot from them through their personal and scholarly discussions, kind company, their suggestions at various points of my research. I would like to thank *Dr. Manikankana Gautam* and *Anuraj Gautam* for providing me with their kind affection, care and hospitality at IISERM.

I would like to thank my friends at IISERM: *Sayan*, *Raju*, *Somnath*, *Joydip*, *Daimiota*, *Virender*, *Sandeep*, *Parth*, *Abhishek*, *Mamta*, *Swati*, *Debopriya*, *Ipsita*, *Anjali*, *Alkit*, *Amartya*, *Soumitro*, *Vickram*, *Pinku*, *Uttam*.

I am very much indebted to my family, with gesture of gratitude to my dear parents for their love, affection and supporting me in all pursuits. I express my love to my dear brother for making me smile at most difficult times. As importantly, my special thanks to *Swagata Bhattacharyya* for always being there for me during my ups and downs.



## List of Figures

- Figure 1.3-** Schematic of various redox processes associated with photocatalysis.
- Figure 1.4-** Band positions of some visible-light responsive photocatalysts and the redox potentials for water splitting at  $pH = 7$  in aqueous solution.
- Figure 1.5-** Schematic of photocatalytic reaction and charge transfer pathways involved with Ag/AgBr/BiOBr heterostructures under visible light illumination.
- Figure 1.6-** Band gap of a metal doped semiconductor.
- Figure 3.2-** Probable formation mechanism of hierarchical BiOX Microspheres.
- Figure 4.1-** PXRD patterns of (a) BiOCl, (b) BiOBr and (c) BiOI.
- Figure 4.2-** PXRD patterns of (a)  $Bi_4TaO_8Cl$ , (b)  $Bi_4TaO_8Br$  and (c)  $Bi_4TaO_8I$
- Figure 4.3-** SEM images of (a) BiOCl, (b) BiOBr, (c) BiOI, (d)  $Bi_4TaO_8Cl$ , (e)  $Bi_4TaO_8Br$  and (f)  $Bi_4TaO_8I$ .
- Figure 4.4-** DRS plots of (a)  $Bi_4TaO_8Cl$ , (b)  $Bi_4TaO_8Br$  and (c)  $Bi_4TaO_8I$ .
- Figure 4.5-** Crystal Structure of  $Bi_4TaO_8X$  consisting of Sillen and Aurivillius blocks.
- Figure 4.6-** Mott-Schottky plot of  $Bi_4TaO_8Br$  in 0.1 M  $Na_2SO_4$  solution ( $pH=2$ ).
- Figure 4.7-** Chemical Structure of Rhodamine B.
- Figure 4.8-** Temporal UV-Vis spectra of RhB conversion to Rh110 using  $Bi_4TaO_8Br$  under visible light irradiation.
- Figure 4.9-**  $pH$  dependent percentage yield of RhB conversion to Rh110 using  $Bi_4TaO_8Br$ .
- Figure 4.10-** Photoluminescence spectra of RhB solution (a) before and (b) after photoirradiation.
- Figure 4.11-** HRMS spectra collected at different intervals (a) 0 min (b) after 45 min photoirradiation.
- Figure 4.12-** HRMS spectra collected at different intervals: after 110 min (a) and 130 min (b) of photoirradiation.
- Figure 4.13-** Temporal UV-Visible spectra of RhB conversion to Rh110 using  $Bi_4TaO_8Br$  under sunlight irradiation.
- Figure 4.14-** PXRD patterns of Fresh and Regenerated catalyst.
- Figure 4.15-** UV-Visible spectra corresponding to adsorption RhB over a period of 24 hours.

- Figure 4.16-** FTIR spectra of (a)  $\text{Bi}_4\text{TaO}_8\text{Br}$  (b) RhB (c) RhB- $\text{Bi}_4\text{TaO}_8\text{Br}$  after photoirradiation.
- Figure 4.17-** Fluorescence decay kinetics of (a) RhB and (b) solution after photoirradiation.
- Figure 4.18-** PXRD patterns of prepared  $\text{M@Bi}_4\text{TaO}_8\text{Br}$ .
- Figure 4.19-** FE-SEM micrographs of (a)  $\text{Ag@Bi}_4\text{TaO}_8\text{Br}$  (b)  $\text{Pd@Bi}_4\text{TaO}_8\text{Br}$  and (c)  $\text{Pt@Bi}_4\text{TaO}_8\text{Br}$ .
- Figure 4.20-** Elemental composition of (a)  $\text{Ag@Bi}_4\text{TaO}_8\text{Br}$  (b)  $\text{Pd@Bi}_4\text{TaO}_8\text{Br}$  and (c)  $\text{Pt@Bi}_4\text{TaO}_8\text{Br}$  obtained from EDS studies.
- Figure 4.20-** DRS patterns of  $\text{M@Bi}_4\text{TaO}_8\text{Br}$  and bare  $\text{Bi}_4\text{TaO}_8\text{Br}$ .
- Figure 4.21-** Tauc plot of  $\text{M@Bi}_4\text{TaO}_8\text{Br}$  and bare  $\text{Bi}_4\text{TaO}_8\text{Br}$ .
- Figure 4.22-** Photoluminescence spectra of  $\text{M@Bi}_4\text{TaO}_8\text{Br}$  and bare  $\text{Bi}_4\text{TaO}_8\text{Br}$ .
- Figure 4.23-** Temporal UV-Visible spectra showing RhB degradation by Metal loaded and bare  $\text{Bi}_4\text{TaO}_8\text{Br}$ .
- Figure 4.24-** Photocatalytic RhB degradation by Metal loaded and bare  $\text{Bi}_4\text{TaO}_8\text{Br}$ .
- Figure 4.25-** Plot of  $\ln(C_0/C_t)$  as a function of irradiation time in the cases of  $\text{M@Bi}_4\text{TaO}_8\text{Br}$ , bare  $\text{Bi}_4\text{TaO}_8\text{Br}$  and P25  $\text{TiO}_2$ .
- Figure 4.26-** Plot showing percentage degradation of RhB by  $\text{M@Bi}_4\text{TaO}_8\text{Br}$ , bare  $\text{Bi}_4\text{TaO}_8\text{Br}$  and P25  $\text{TiO}_2$ .
- Figure 4.27-** Plot of cyclic stability test for degradation of RhB by  $\text{Pd@Bi}_4\text{TaO}_8\text{Br}$ .
- Figure 4.28-** PXRD patterns of Fresh and regenerated  $\text{Pd@Bi}_4\text{TaO}_8\text{Br}$ .
- Figure 4.29-** HRMS spectra collected at different intervals (a) 0 min; (b) after 10 min; (c) 15 min photoirradiation using  $\text{Pd@Bi}_4\text{TaO}_8\text{Br}$ .
- Figure 4.30-** Percentage of RhB degradation using different scavenger using  $\text{Pd@Bi}_4\text{TaO}_8\text{Br}$ .
- Figure 4.31-** Schematic representation of the photocatalytic RhB degradation mechanism.

## List of Photographs

**Photo 1.1-** (a) Untreated toxic effluents from industry released to water bodies; (b) A river turned into a toxic pool of dyes released from industries.

**Photo 1.2-** (a) Excessive spraying of insecticides causes eutrophication; (b) Water runoffs from an agricultural land.

**Photo 2.1-** RhB converted to Rh110 after 130 min photoirradiation (a) in normal light; (b) under UV chamber

**Photo 2.1-** Images of Rh110 obtained by photoirradiation of RhB after 130 min (a) in normal light and (b) the same in an UV chamber.

**Photo 2.2-** Photocatalytic degradation of RhB solution by  $M@Bi_4TaO_8Br$ .

**Photo 3.1-** Schematic illustration showing solvothermal synthesis of BiOX.

**Photo 3.3-** Schematic illustration of the synthesis of  $Bi_4TaO_8X$  via solid-state route.

## **List of Tables**

**Table 1.1-** Permissible limits for the disposal of wastewaters

**Table 1.2-** Advantages and disadvantages of various conventional treatment processes

**Table 3.1-** Commercial Cost of common Rhodamine Dyes

**Table 4.1-** Lattice parameters of  $\text{Bi}_4\text{TaO}_8\text{X}$

## Notation

°C	Centigrade
Approx.	Approximately
DRS	Diffuse Reflectance Spectroscopy
FE-SEM	Field Emission Scanning Electron Microscopy
FTIR	Fourier-Transform Infrared Spectroscopy
g	Grams
h	Planck's constant
h	Hours
HRMS	High-Resolution Mass Spectrometry
K	Kelvin
k	Rate Constant
kHz	Kilohertz
M	Molarity
M@Bi <sub>4</sub> TaO <sub>8</sub> Br	Metal loaded Bi <sub>4</sub> TaO <sub>8</sub> Br
Min	Minutes
mL	Millilitre
mM	Millimolar
nm	Nanometre
PL	Photoluminescence
PXRD	Powder X-ray Diffraction
Rh110	Rhodamine 110
RhB	Rhodamine B
rpm	Revolutions per minute
s	Seconds
UV-Vis	UV-Visible Spectroscopy
V	Volt
λ	Wavelength
μM	Micromolar
v	Frequency
τ	Fluorescence Lifetime





# Contents

List of Figures .....	i
List of Photographs .....	iii
List of Tables.....	iv
Notation .....	v
Abstract .....	vii
1. INTRODUCTION.....	1
2. SCOPE OF THE PRESENT STUDY .....	17
2.1 Photocatalytic transformation of Rhodamine B to Rhodamine 110.....	17
2.2 Photocatalytic dye degradation by metal loaded Bi <sub>4</sub> TaO <sub>8</sub> Br .....	20
3. EXPERIMENTAL SECTION .....	22
4. RESULTS AND DISCUSSIONS.....	27
4.1 Photocatalytic transformation of Rhodamine B to Rhodamine 110.....	27
4.2 Photocatalytic dye degradation by metal loaded Bi <sub>4</sub> TaO <sub>8</sub> Br .....	42
5. CONCLUSION .....	55
6. SCOPE OF FUTURE WORK.....	56
7. BIBLIOGRAPHY .....	57



## Abstract

The advent of heterogeneous catalysis has facilitated the solar assisted toxic pollutant removal and synthesis of fine chemicals. Mixed anion compounds are known to be effective photocatalyst for visible light-induced water splitting, but the available materials have been almost limited to oxynitrides and oxysulfides. In this thesis we have synthesised, single layer Sillen–Aurivillius perovskite tantalum based oxyhalide  $\text{Bi}_4\text{TaO}_8\text{X}$  ( $\text{X} = \text{Cl}, \text{Br}, \text{I}$ ) and metal loaded  $\text{Bi}_4\text{TaO}_8\text{Br}$  ( $\text{M}@\text{Bi}_4\text{TaO}_8\text{Br}$ ). The materials were prepared using conventional solid-state route and photodeposition of metals onto  $\text{Bi}_4\text{TaO}_8\text{Br}$ . The prepared catalysts were characterised by PXRD, FE-SEM and DRS, which inferred they were single phase, micrometre sized particles with band gap in the visible region.

The prepared photocatalyst  $\text{Bi}_4\text{TaO}_8\text{Br}$  was used to convert RhB to Rh110 under visible light and sunlight irradiation. We observed ~40% yield at  $\text{pH}=7$ , and the percentage yield being  $\text{pH}$  dependent. The photocatalysts exhibited excellent stability under visible light irradiation as evident from the cyclic stability tests of 50 cycles in the case of RhB to Rh110. We also examined the photocatalytic activity of the prepared  $\text{M}@\text{Bi}_4\text{TaO}_8\text{Br}$  by degradation of RhB under visible light illumination. We observed the excellent activity of the  $\text{Pd}@\text{Bi}_4\text{TaO}_8\text{Br}$  with a rate constant of  $0.35372 \text{ min}^{-1}$  surpassing commercial state-of-the-art P25  $\text{TiO}_2$  ( $0.10359 \text{ min}^{-1}$ ) by 3.4 times. Such high activity of Pd loaded catalyst is believed to be due to the presence of various active sites on its surface, owing to efficient electron transfer from CB of catalyst to the Fermi level of Pd which helps in effective separation of electron-hole pairs.  $\text{Pd}@\text{Bi}_4\text{TaO}_8\text{Br}$  is superior to current commercial catalysts, in terms of catalytic efficiency and recycling stability which indicated the possibility of realising industrial scale use of toxic pollutant removal under solar irradiation.

The valence band maximum of  $\text{Bi}_4\text{TaO}_8\text{Br}$  is unusually high, owing to highly dispersive O-2p orbitals (and not Br-4p orbitals), affording a narrow band gap and enhanced stability against photocorrosion. This study suggests that Sillen–Aurivillius perovskite oxyhalides is a promising system for versatile band level tuning for establishing efficient water oxidation under visible light.



## 1. INTRODUCTION

*“Thousands have lived without love, not one without Water!”* - W.H. Auden

Water, as defined by Cambridge Dictionary, is “a clear liquid, without colour or taste that falls from the sky as rain and is necessary for animal and plant life”. Water covers the two-thirds of the earth's surface and human body consists of 75% of it. Hence it is one of the essential elements responsible for life on earth. However, due to increased industrialization and urbanization, there has been a surge in the discharge of a large number of toxic wastes into the water bodies. Some types of the wastewater include:

- ❖ Sewage Waste: Sewage, garbage and liquid waste of households, agricultural lands and industries are discharged into lakes and rivers consisting harmful chemicals and toxins.
- ❖ Illegal Dumping: Dumping of solid wastes and litters in water bodies causes enormous problems. Litters include glass, plastic, aluminium, Styrofoam cups etc.
- ❖ Industrial Waste: Industrial waste contains pollutants like asbestos, lead, mercury, toxic dyes and petrochemicals which are incredibly harmful to both people and environment.
- ❖ Oil Spill: Seawater gets polluted due to oil spilt from ships and tankers the spilt oil does not dissolve in water and forms a thick sludge polluting the marine ecosystem.

Eventually, there are two choices to overcome these problems. Firstly, prevention and control by adopting various strategies to minimise the waste generation and secondly, by the development of different treatment methods.

Industrial wastewater consists of both organic and inorganic nature including toxic substances like dyes and pigments, which are discharged without treatment. Dyes may be classified according to the chemical structure or by their usage or based on application method. Broad classifications can be 1) Natural Dyes 2) Synthetic Dyes. Natural dyes are those derived from plants, invertebrates, or minerals. The majority of these dyes come from plant sources such as roots, barks, leaves etc. Synthetic dyes are derived from organic or inorganic compounds. Examples of this class of dyes are Direct, Acid, Basic, Reactive dyes etc.

## **1.1 Classification of dyes**

The correct system for the classification of dyes is by its chemical structure, which has many advantages. Firstly, it helps in identifying dyes as belonging to a group that has characteristic properties, for example, azo dyes or xanthene dyes. The types of dyes are listed below:

### **1.1.1 Acidic dye**

Acidic dyes are highly water-soluble dyes contain  $-\text{SO}_3\text{H}$  groups, which are usually present as sodium sulphonate salts. Under acidic condition, the  $-\text{NH}_2$  functionalities of the fibres are protonated to give a positive charge:  $-\text{NH}_3^+$ . This charge interacts with the negative counterpart, allowing the formation of ionic interactions. As well as this, van der Waals bonds, dipolar bonds and hydrogen bonds are formed between dye and fibre. Example- Nigrosine, Eosin, India Ink etc.

### **1.1.2 Basic Dye**

Basic dyes consist of cationic functional groups such as  $-\text{NR}_3^+$  or  $=\text{NR}_2^+$ . The common anionic group attached to acrylic polymers is the  $-\text{SO}_3^-$ , closely followed by the carboxylate group,  $-\text{CO}_2^-$ . These can be introduced as a result of co-polymerisation, or by the residues of anionic polymerisation inhibitors. It is this anionic property which makes acrylic polymers suitable for dyeing with acidic dyes since a strong ionic interaction between dye and polymer exists. Examples-Crystal Violet, Methylene Blue, Safranin etc.

### **1.1.3 Reactive Dye**

Reactive dyes utilise a light absorbing unit attached to a substituent that is capable of directly responding with the fibre substrate. The covalent bonds that attach the reactive dye to natural fibres make them among the most noticeable of dyes. Reactive dyes, such as Procion MX, Cibacron F etc. can be used in ambient conditions. These dyes are the best choice for dyeing cotton and other cellulose fibres for domestic purposes.

### **1.1.4 Disperse dye**

Disperse dyes are prepared by dyeing of cellulose acetate, and these are water-insoluble dyes. These dyes are finely ground in the presence of a dispersing agent and are commercially available as the powder. The primary applications of these dyes are

in dyeing polyester, nylon, cellulose triacetate, and even acrylic fibres. Examples- C.I. Disperse Violet 4, C.I. Disperse Red 15 etc.

### **1.1.5 Azo Dye**

Azo dyes can supply a complete rainbow of colours, mainly aromatic. The name 'azo' comes from the -N=N- group by making it part of an extended delocalized system consisting aromatic moieties. Azo dyes are most abundant and most versatile dyes. High stability in heat and during washing and resistance to the microbial activity made them dearer for industrial use. Most of the azo dyes contain one azo group, but some contain two, three or more. The bright colour is due to the azo bonds and chromophores; they do not occur naturally. Examples- Methyl Orange, Direct Blue 1 etc.

### **1.1.6 Xanthene Dye**

Xanthene dyes are those containing the xanthylium or dibenzo- $\gamma$ -pyran nucleus (xanthene) as the chromophore with amino or hydroxy groups meta to the oxygen as the usual auxochromes. They are essential because of their excellent colours absorption properties in the visible light. As a consequence of their rigid chromophoric nucleus, xanthenes are often fluorescent, which also adds to their strength and brightness, but, as is often the case with fluorescent dyes, they have lower lightfastness compared to other dyes. Examples are Rhodamine B, Rhodamine 110, Pyronine B etc.

## **1.2 Water Pollution from Dyeing Industries**

The use of dyes has enormously increased during the last two decades. A large number of organic chemicals, salts of heavy metals such as Zn, Pb, Cr, Cu, Hg, Ba, weak acids and alkalis are required for the manufacture of dyes. In addition the other industries such as textile, plastics, paper and pulp also generate effluents containing toxic organic dyes. Dyes from the textile industries pollute the environment due to its intense colour and carcinogenicity. This has become an issue of a worldwide concern. Reactive intermediates formed from the dyes also initiate the morphological and genetic alterations, thereby making the dye cytotoxic and carcinogenic<sup>[1]</sup>. In addition, the release of these dye effluents causes eutrophication which perturbs aquatic ecosystems. The main intermediates used are benzoic acid, nitrobenzene, chlorobenzene and aniline which are ranked as highly toxic and suspected carcinogens.



**Photo 1.1-** (a) *Untreated toxic effluents from industry released to water bodies;* (b) *A river turned into a toxic pool of dyes released from industries.*

### 1.3 Water Pollution From Agricultural Sector

A pesticide is a substance or mixture of substances intended for preventing, destroying, repelling or mitigating any pest (insect, rodent, nematode, fungus and weed). At present, there are more than 10,000 different pesticides. They are broadly classified according to their general chemical nature into several principal types:

- ❖ Herbicides - meant for killing weeds or undesirable vegetation.  
Example – Alachlor
- ❖ Fungicides- toxic to moulds (fungi) and check plant disease.  
Example – Thiram
- ❖ Insecticides- designed to kill insects in crops.  
Example – Malathion

When the agro-chemicals are discharged to the main water bodies without any prior treatment, they can cause havoc to the ecological balance in the environment as these molecules have carcinogenic and mutagenic properties towards aquatic organisms and thus pose a threat to human life at the end of the food chain<sup>[2,3]</sup>. Thus, it is pertinent to develop method to counteract these problems by adopting suitable techniques.





**Photo 1.2** - (a) Excessive spraying of insecticides causes eutrophication; (b) Water runoffs from an agricultural land.

#### 1.4 TREATMENT TECHNIQUES FOR DEGRADATION OF POLLUTANTS

For mitigating the pollution related problems a tremendous surge of research is been carried out to develop new cost-effective and robust methods of purifying water and simultaneously minimising the use of toxic chemicals and its impact on the environment. Thus to protect the water resources, Indian government has set forth limits for different water bodies<sup>[4]</sup>. The permissible limits for waste water are listed in Table 1.1.

**Table 1.1** : Permissible limits for the disposal of wastewaters<sup>[5]</sup>

Parameters	Into inland surface waters	Into public sewers	On land for irrigation
pH	5.5-9.0	5.5-9.0	5.5-9.0
Biological oxygen demand (for 5 days at 20 °C) (mg/L)	30	350	100
Chemical oxygen demand (mg/L)	250	-	-

<b>Suspended solids (mg/L)</b>	<b>100</b>	<b>600</b>	<b>200</b>
<b>Total dissolved solids (inorganic) (mg/L)</b>	<b>2100</b>	<b>2100</b>	<b>1000</b>
<b>Temperature (°C)</b>	<b>40</b>	<b>45</b>	<b>-</b>
<b>Phenolic compounds (mg/L)</b>	<b>1</b>	<b>5</b>	<b>-</b>
<b>Cyanides (mg/L)</b>	<b>0.2</b>	<b>2</b>	<b>0.2</b>
<b>Sulphides (mg/L)</b>	<b>2</b>	<b>-</b>	<b>-</b>
<b>Fluorides (mg/L)</b>	<b>2</b>	<b>15</b>	<b>-</b>
<b>Total residual chlorine (mg/L)</b>	<b>1</b>	<b>-</b>	<b>-</b>
<b>Cadmium (mg/L)</b>	<b>2</b>	<b>1</b>	<b>-</b>
<b>Mercury (mg/L)</b>	<b>0.01</b>	<b>0.01</b>	<b>-</b>

Many physicochemical methods such as coagulation, precipitation, adsorption, membrane filtration and oxidation have been tried for treatment of contaminated effluent. The different conventional treatment techniques are discussed below:

#### ❖ **Coagulation**

Surface waters contain suspended and colloidal solids from land erosion, decaying vegetation and microorganisms. Salt and silt are considered as a coarser material and can be removed by filtration whereas finer particles must be chemically coagulated to produce larger floc which can be removed by subsequent settling and filtration. Commonly used coagulants are aluminium sulphate, potash alum, ammonia alum, ferrous sulphate and ferrous chloride<sup>[6,7]</sup>.

#### ❖ **Ion Exchange Processes**

An insoluble resin can be used to remove ions both positive and negative charges and releases other ions of similar charge into solution with no structural changes in the resin. They remove specific anions such as nitrate, fluoride, arsenic, magnesium and calcium.

The exchange resins are organic polymer beads usually in size range of 0.3 to 1.4. mm diameter with the specific gravity of 1.3 to 1.4<sup>[8]</sup>.

#### ❖ **Membrane Filtration**

Membrane filtration processes used to remove colloidal and particulate contaminants. The RO and NF processes use semi-permeable membranes to separate dissolved salts, organic molecules and metal ions. The application of different membrane systems is based on pore size for removal of contaminants. The membrane process which uses a membrane with pore size of 0.1 to 0.7  $\mu\text{m}$  is referred to as microfiltration (MF), and when the pore size range is 0.008 to 0.8  $\mu\text{m}$ , it is called ultrafiltration (UF). The membrane process in the pore size range of 0.005 to 0.008  $\mu\text{m}$  is called as nanofiltration (NF) and 0.0001 to 0.007  $\mu\text{m}$  for reverse osmosis (RO). These two processes include the removal of aqueous salts, dissolved organic compounds and metal ions<sup>[9,10]</sup>.

### **1.5 Drawbacks of Conventional Treatment processes**

Biological treatment would be cost effective, but most of the dyes are resistant to biological degradation. This treatment may remove BOD (Biological Oxygen Demand), COD (Chemical Oxygen Demand), and suspended solids but is ineffective in removing the colour of dyes<sup>[11]</sup>. Thermal and non-thermal processes have been used to treat the organic wastes, and they have their limitations<sup>[12,13]</sup>. By using chemical coagulation method, the azo dyes cannot be removed due to their hydrophilic property<sup>[14]</sup>.

Physicochemical methods such as coagulation and flocculation produce large amounts of sludge which creates disposal problems<sup>[15]</sup>. Electrolytic precipitation, foam fractionation and micro-filtration are rather expensive from the economic point of view. Aerobic processes are not suitable to remove azo dyes due to the electron withdrawing nature of the azo bonds<sup>[16]</sup>. Chlorination and ozonation are also being used for the treatment of textile effluents. Though these techniques remove the colour and organics, the process is not economically viable<sup>[17]</sup>. Some general advantages and disadvantages of various physical and chemical treatment processes are listed in Table 1.2.

**Table 1.2-** Advantages and disadvantages of various conventional treatment processes

<b>Physical/Chemical Methods</b>	<b>Merits</b>	<b>Demerits</b>
<b>Flocculation/Coagulation</b>	Rapid Process	High energy costs and formation of by products
<b>Adsorption</b>	Good removal of a wide range of dyes	Adsorbent requires regeneration or disposal
<b>Oxidation</b>	Removes all dye types	Concentrated sludge production
<b>Membrane based Technologies</b>	Economically feasible	High sludge production

Hence, a sensible approach is needed to degrade the harmful pollutants. One such approach is implementing Advanced Oxidation Process (AOP) for abatement of pollution.

### 1.6 Advanced Oxidation Process (AOP)

Treatment using Advanced Oxidation Process (AOP) has proven to be a promising technology by various researchers for the degradation of harmful pollutants such as dyes, insecticides, endocrine disruptors, phenols etc.

Advanced Oxidation Processes include the following methods:

- ❖ Photolysis (UV or UV-Vis)
- ❖ Hydrogen peroxide
  - a)  $\text{H}_2\text{O}_2 + \text{UV}$
  - b) Fenton:  $\text{H}_2\text{O}_2 + \text{Fe}^{2+}/\text{Fe}^{3+}$
  - c) Photo Fenton:  $\text{H}_2\text{O}_2 + \text{Fe}^{2+}/\text{Fe}^{3+} + \text{UV}$
- ❖ Ozone (Ozonation, Photo-ozonation, Ozonation+catalysis)
- ❖ Photocatalysis (using semiconductor oxide catalysts-  $\text{TiO}_2$ ,  $\text{Ag}_3\text{PO}_4$ , etc.,)

This thesis deals with the photocatalytic route of AOP, so that we will discuss only photocatalysis in detail.

## 1.7 Photocatalysis

The International Union of Pure and Applied Chemistry (IUPAC) has defined a catalyst as — “A substance that increases the rate of a reaction without modifying the overall standard Gibbs energy change in the reaction”<sup>[18]</sup>. The catalyst is both a reactant and a product of the reaction, i.e., the catalyst is restored after each catalytic action. Furthermore, the catalyst does not influence the thermodynamical equilibrium composition after the cessation of the reaction. Photocatalysis is another branch of catalysis which makes use of both light and catalyst. Verhoeven<sup>[19]</sup> defined photocatalysis as a change in the rate of a chemical reaction under the action of light in the presence of photocatalysts that absorb light quanta and are involved in the chemical transformations of the reaction participants. Water treatment using photocatalytic technology<sup>[20]</sup>, has attracted much attention in recent years<sup>[21-25]</sup>. The field of photocatalysis has grown enormously since the demonstration of photocatalytic water splitting on TiO<sub>2</sub> by Fujishima and Honda<sup>[26]</sup> in 1972. Frank & Bard<sup>[27]</sup> reported the reduction of CN<sup>-</sup> in water which led to increasing the research for pollution abatement using solar energy. Kabra<sup>[28]</sup> *et al.* listed such advantages of photocatalysis and they are:

- Photocatalysis is an alternative for the energy intensive conventional treatment techniques utilising renewable solar energy.
- Conventional treatment methods transfer pollutants from one medium to another whereas photocatalysis results in the formation of innocuous products.
- A vast number of contaminants present in different water bodies can be detoxified by this method.
- Pollutants in any physical state (solid, liquid and gas) can be treated by this method.
- Mild reaction conditions and recovery of the catalysts make this technique a greener one and hence does not burden the environment and
- As this technique converts the pollutants into CO<sub>2</sub> and mineral salts, secondary waste generation is minimal.

In all the photocatalytic oxidation processes a semiconductor either in the form of oxide, nitride, sulphide or oxyhalide, oxynitrides are used. Hoffmann<sup>[29]</sup> *et al.* reviewed

environmental applications of a considerable number of semiconductors. He concluded that semiconductor photocatalysis appears to be a promising technology for air purification, water disinfection, hazardous waste remediation, and water purification.

### 1.7.1 Semiconductor Photocatalysis

When a semiconductor is irradiated with photons whose energy equals or exceeds its bandgap energy, electrons ( $e^-$ ) are promoted to the conduction band, leaving positive holes ( $h^+$ ) in the valence band, and these holes and electrons act as oxidizing and reducing agents respectively<sup>[30]</sup>. Holes react with hydroxyl groups present in the water and produce strong oxidizing OH- radicals. On the other hand, electrons react with adsorbed molecular oxygen yielding superoxide radicals<sup>[31]</sup>  $O_2^-$ .

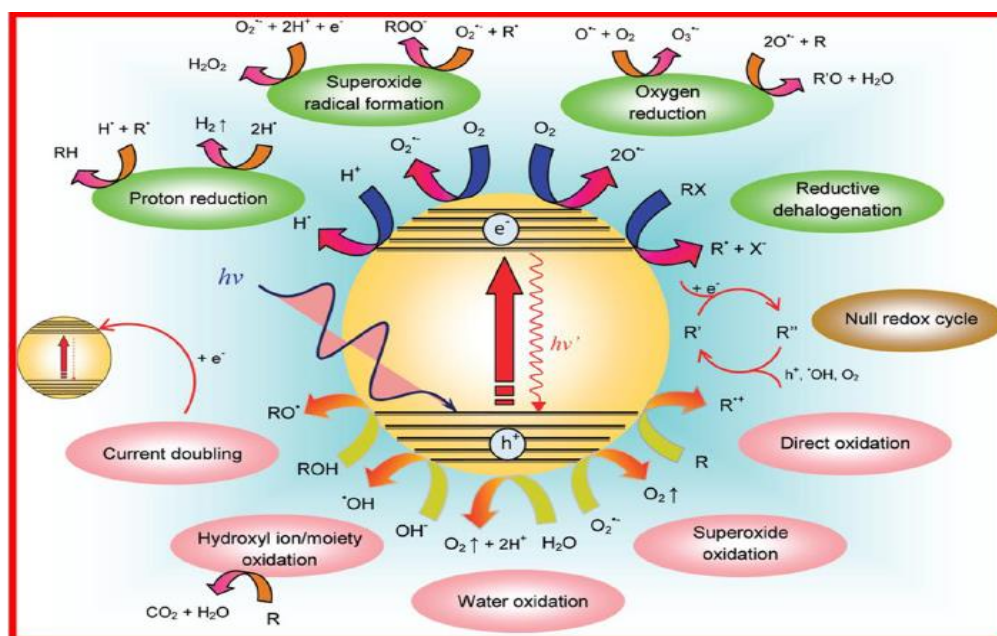


**Fig 1.3-** Various redox processes assisted by photocatalysis

These hydroxyl radicals and superoxide radicals act as powerful oxidizing agents. The formation of these radicals is governed by the conduction (CB) and valence (VB) band potentials of the photocatalyst with respect to the redox potential of the surface reaction. Unless the excited high energy photoelectrons are used up before their rapid recombination to the conduction band edge, it is not possible to catalyse a reduction reaction where the reduction potential is more negative than the CB. Likewise, it is difficult to catalyse an oxidative reaction where the reduction potential is more positive than the VB<sup>[32]</sup>.

Semiconductors such as ZnO, TiO<sub>2</sub>, Fe<sub>2</sub>O<sub>3</sub>, WO<sub>3</sub>, SnO<sub>2</sub>, ZrO<sub>2</sub>, CdS, SrTiO<sub>3</sub>, Ag<sub>3</sub>PO<sub>4</sub>, ZnS etc. are known to be good photocatalysts for dye degradation studies owing to their electronic structure characterised by a filled valence band and an empty conduction band<sup>[33]</sup>. But the energy gaps were different for different photocatalysts. The bandgap energies of widely used semiconductors are shown in Figure 1.4.

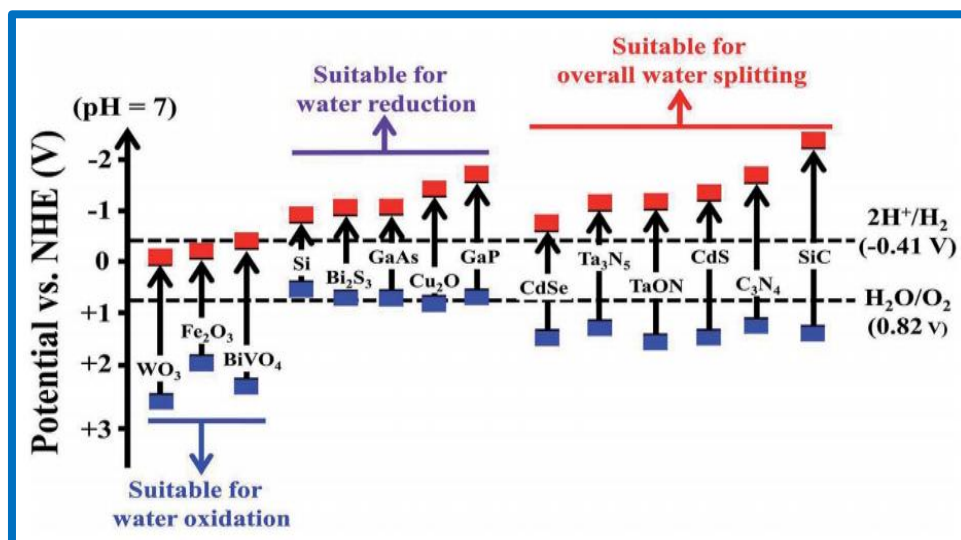


**Fig 1.4-** Band positions of some visible-light photocatalysts and the redox potentials of water splitting at pH =7 in aqueous solution<sup>[34]</sup>

### 1.7.2 Z-scheme Photocatalysis

A system consisting of two photocatalytic reactions connected with a redox mediator has been called a — “Z-scheme” reaction system and it has been employed mostly for the splitting of water. Various researchers reported that “Z-scheme system” in the combined structure involves two-step excitation process which is similar to the photosynthesis of plants<sup>[35–37]</sup>. In the Z-scheme photocatalysis shown by Ag/AgBr/BiOBr<sup>[38]</sup> catalyst is shown in Figure 1.5.

In this catalyst, the excitation of AgBr and BiOBr occurs first. The excited electrons from BiOBr flow into metallic silver through the Schottky barrier, because the CB potential of BiOBr is more negative than the Fermi level of silver. At the same time the Fermi level of silver is more positive than the VB of AgBr. Due to this, electrons flow from silver to VB level of AgBr.

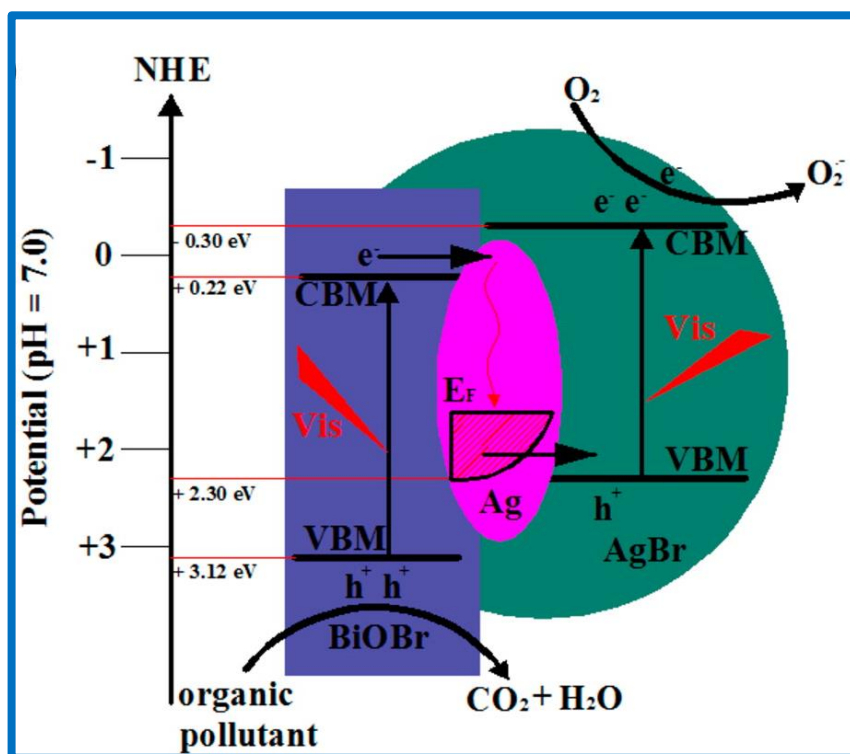


**Fig 1.5-** Schematic of photocatalytic reaction process and charge transfer processes involving the Ag/AgBr/BiOBr hybrid under visible light illumination

These two electrons transfers ( $\text{BiOBr}_{\text{CB}} \rightarrow \text{Ag}$  &  $\text{Ag} \rightarrow \text{AgBr}_{\text{VB}}$ ) prevent the electron/ hole recombination and separates the holes in the VB of BiOBr and electrons in the CB of AgBr. Therefore Ag/AgBr/BiOBr Z-scheme photocatalyst has shown an improved photocatalytic activity. Similar Z-scheme photocatalysis was reported by a lot of researchers<sup>[37,39-49]</sup>.

### 1.7.3 Metal Modified Semiconductor Oxide Catalysts

Dopants such as noble metals, transition metals have been added to titania catalyst to improve its optical response and to reduce the recombination of photogenerated electrons and photogenerated holes<sup>[50]</sup>. The lifetimes of electrons and holes must be long enough to allow them to reach the surface of the photocatalyst in any photocatalytic reaction. The addition of transition metal ions produces new trapping sites which affect the lifetime of the charge carriers. A lifetime of 89.3 ms has been reported for pure titania, whereas doping reduces this lifetime considerably. Noble metals have high



resistance to corrosion and oxidation in moist air unlike most base metals and hence have been used as dopants for titania.

The primary objective of doping is to induce a bathochromic shift, i.e. a decrease of the bandgap or introduction of intra-bandgap states which results in more visible light absorption as shown in Figure 1.6 and 1.7.

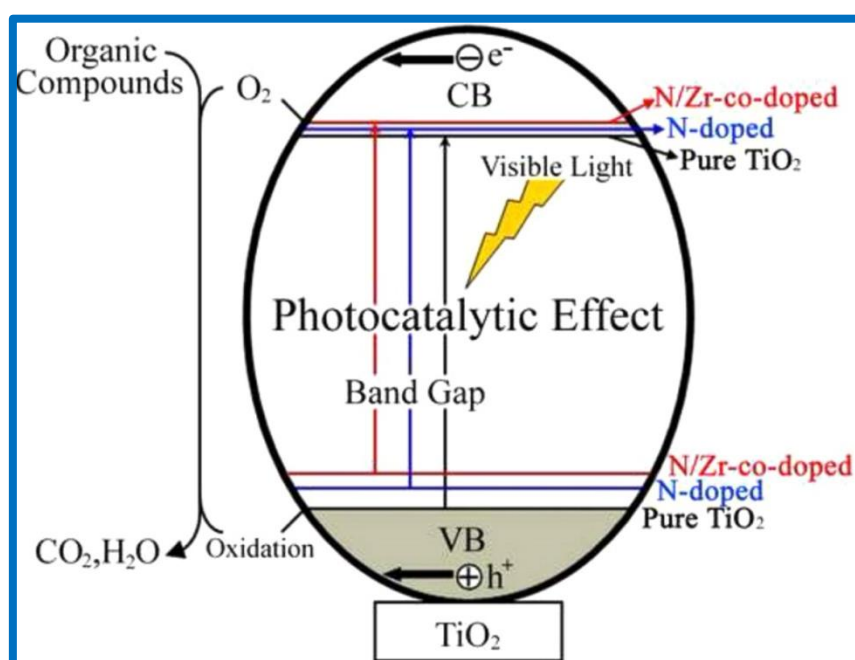


**Fig 1.6-** Band gap of metal doped semiconductor<sup>[51]</sup>

Depending on the type of dopants (co-catalyst) and their concentration, they can allow the light absorption to be widened into the visible region. The overlap of the conduction band due to Ti(3d) with d levels of the transition metals causing red shift of the band edge of TiO<sub>2</sub>. The ionic radii of the host material should have similar size of the dopant ion. Then only the metals can be easily incorporated into the crystal lattice of TiO<sub>2</sub>.

For example, the ionic radii of Ni<sup>2+</sup>= 0.72 Å, Zn<sup>2+</sup>= 0.74 Å, Cr<sup>3+</sup>= 0.76 Å and Fe<sup>3+</sup>= 0.69 Å are quite similar to that of the host Ti<sup>4+</sup>=0.75 Å ions and they can easily be doped in to titania lattice<sup>[52]</sup>. Zaleska<sup>[53]</sup> *et al.* reviewed the effect of doping of TiO<sub>2</sub> and reported that the titanium dioxide is an effective photocatalyst for water and air purification and for self-cleaning surfaces. She suggested the process of visible light-activated TiO<sub>2</sub> could be prepared by metal-ion implantation, reduction of TiO<sub>2</sub>, non-metal doping or sensitising TiO<sub>2</sub> with dyes.

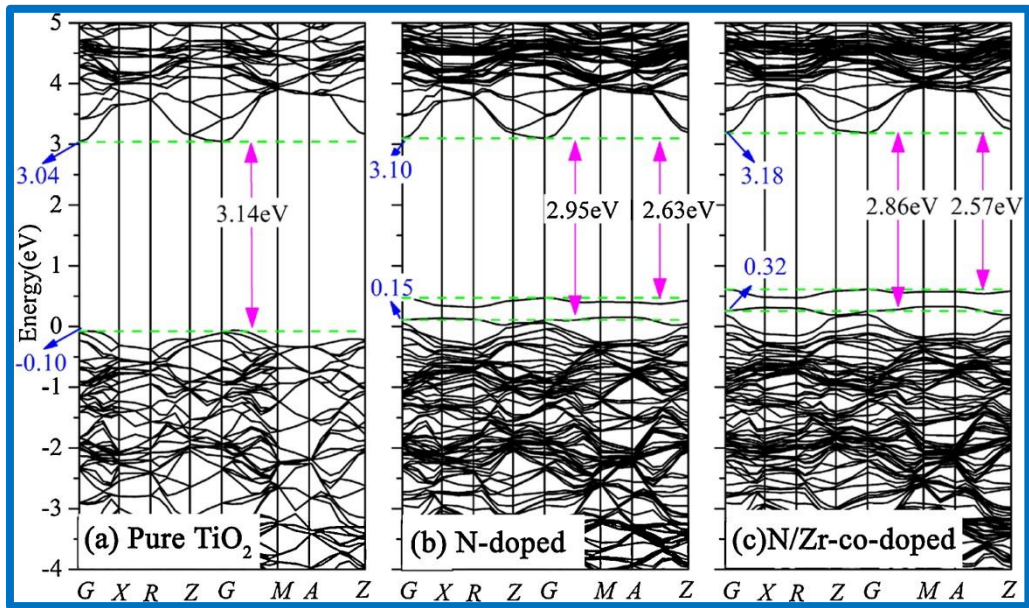


**Fig 1.7-** The band structure of: (a) pure  $\text{TiO}_2$ , (b) N-doped  $\text{TiO}_2$  and (c) N/Zr-co-doped  $\text{TiO}_2$  calculated with GGA + U method. The highest occupied state of pure  $\text{TiO}_2$  is chosen as its Fermi energy and is set to zero. The band gap value has been marked on the figures the band gap of pure, N-doped and N/Zr co-doped  $\text{TiO}_2$  calculated are 3.14 eV, 2.94 eV and 2.86 eV respectively<sup>[51]</sup>

The paper also reviewed the preparation methods of doped- $\text{TiO}_2$  with metallic and non-metallic species, including various types of dopants and doping methods currently available and also discussed the mechanism of heterogeneous photocatalysis in the presence of  $\text{TiO}_2$ . Numbers of researchers have studied the different metal doped/impregnated  $\text{TiO}_2$  catalysts towards the degradation of harmful pollutants and they are given in the following section. Huang<sup>[54]</sup> *et al.* showed that platinum deposits on  $\text{TiO}_2$  trap photo-generated electrons, and subsequently increase the photo-induced electron transfer rate at the interface. Behnajady<sup>[55]</sup> *et al.* studied and compared the effect of silver catalysts prepared by liquid impregnation method and photodeposition method. The photocatalytic activity of silver doped  $\text{TiO}_2$  was tested by the photocatalytic degradation of C.I. Acid Red 88 (AR88) as a model compound from monoazo textile dyes. Results showed that the silver doped  $\text{TiO}_2$  is more efficient than undoped  $\text{TiO}_2$  at photocatalytic degradation of AR88 and they attributed this due to its ability to trap electrons. This process reduces the recombination of light generated electron-hole pairs at  $\text{TiO}_2$  surface. Barakat<sup>[56]</sup> *et al.* observed higher activity for  $\text{Co}^{2+}$  doped  $\text{TiO}_2$  in the photocatalytic

degradation of 2-chlorophenol and confirmed the significant absorption shift into the visible region compared to pure TiO<sub>2</sub>.

Choi<sup>[57]</sup> *et al.* studied the titanium dioxide (M-TiO<sub>2</sub>), doped with 0.1 to 1.0 % of 13 different metal ions which are silver (Ag<sup>+</sup>), rubidium (Rb<sup>+</sup>), nickel (Ni<sup>2+</sup>), cobalt (Co<sup>2+</sup>), copper (Cu<sup>2+</sup>), vanadium (V<sup>3+</sup>), ruthenium (Ru<sup>3+</sup>), iron (Fe<sup>3+</sup>), osmium (Os<sup>3+</sup>), yttrium (Y<sup>3+</sup>), lanthanum (La<sup>3+</sup>), platinum (Pt<sup>4+</sup>, Pt<sup>2+</sup>), and chromium (Cr<sup>3+</sup>, Cr<sup>6+</sup>) and showed red shift in the absorption bands for some of the doped titania catalysts beyond 400 nm. Mirkhani<sup>[58]</sup> *et al.* reported higher rate constant values in the photocatalytic degradation (PCD) of azo dye over 1% Ag-doped TiO<sub>2</sub> than bare titania under UV irradiation. Xie & Yuan<sup>[25]</sup> investigated the photodegradation of the dye X-3B by Ce<sup>4+</sup> doped TiO<sub>2</sub> under visible light irradiation. They correlated the photoactivity to the particle size, morphology and electron scavenging effect.

## 1.8 Mechanism of photocatalysis

Various redox processes are possible when light shines on the semiconductor materials. The primary semiconductor photocatalytic mechanism proceeds as follows :

- Under UV or visible light illumination of semiconductor, when the photon of radiation is greater than the band gap energy of semiconductor, promotion of electrons from valence band to the conduction band occurs.
- The photoexcited electrons in the conduction band reduce the dissolved oxygen to superoxide ions, which may further react with protons and produces HO<sub>2</sub><sup>•</sup> radicals. These radicals further undergo reaction with superoxide anions yielding H<sub>2</sub>O<sub>2</sub>.
- The holes in the valence band oxidize water to yield reactive hydroxy radicals, which decomposes the organic substrate into carbon dioxide and water.

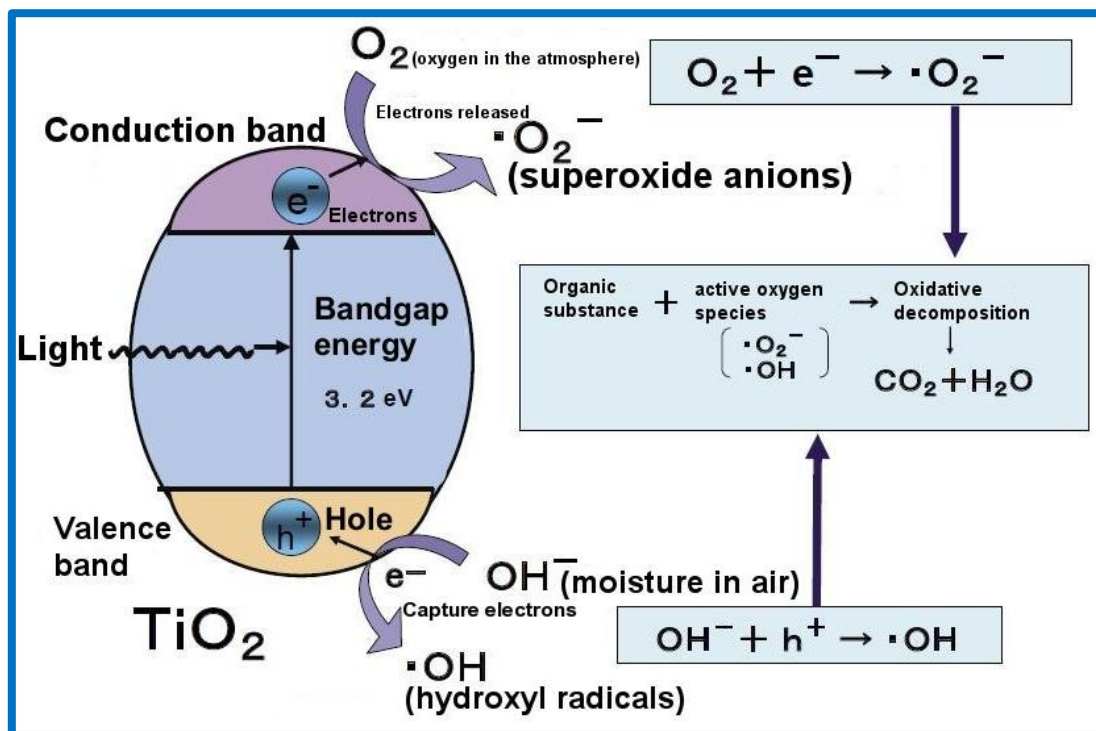


**Fig 1.8-** Mechanism of photocatalytic dye degradation<sup>[32]</sup>

The powerful oxidants such as hydroxyl radical, superoxide radical anion and  $\text{H}_2\text{O}_2$  play essential roles in initiating the oxidative degradation of adsorbed pollutants. The process of degradation proceeds via a number of free radical reactions which produce a large number of intermediates and they undergo simultaneous oxidative cleavage to form  $\text{CO}_2$ ,  $\text{H}_2\text{O}$  and mineral salts. Hence the photogenerated electrons are required to be removed from the surface of the semiconductor to achieve an effective oxidative process.

## 2. SCOPE OF THE PRESENT STUDY

### 2.1 Photocatalytic transformation of Rhodamine B to Rhodamine 110

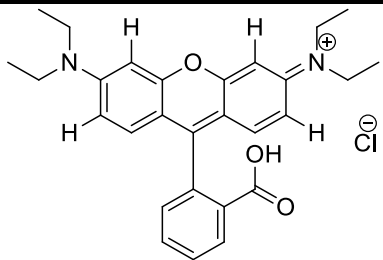
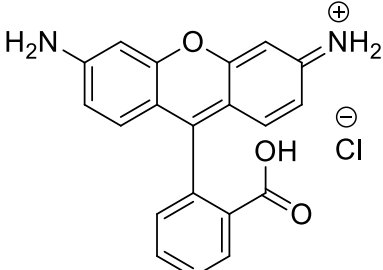
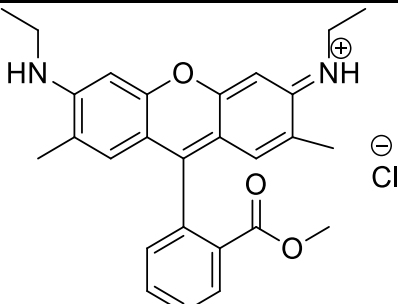
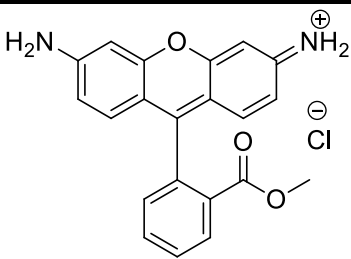
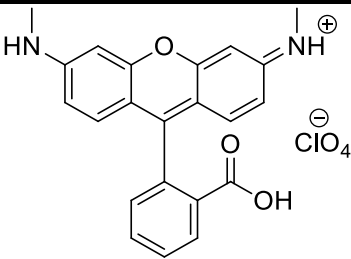
Xanthene based dyes are used for their unique photophysical<sup>[59–62]</sup> properties. Rhodamine 110 being a xanthene dye is likewise known for its unique applications<sup>[63–65]</sup>. Its industrial synthesis is quite challenging due to numerous side product formation during synthesis, leading to difficult separation procedure. Recently, research for the search for latent fluorophores<sup>[66–68]</sup> or pro-fluorophores has been carried out, because of its advantage over “conventional” fluorophores which exhibit bulk fluorescence leading to missing information in biological experiments. Researchers found two crucial yardsticks are indispensable for an efficient pro-fluorophores which are: (a) easy detectability, (b) high reactivity of the bond undergoing cleavage.

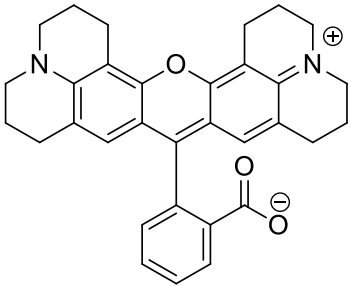
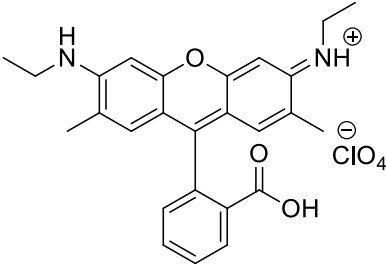
Moreover, among all rhodamine dyes, Rh110<sup>[69–71]</sup> is widely used in this purpose because it carries non-alkylated amino groups which helps easy access to the lone pair of electrons on nitrogen, hence can be easily coupled with carboxylic or acyl groups such as the enzymatic activity of caspase, esterase etc. However, its preparation in pure form is extremely challenging involving low temperature<sup>[72]</sup>, refluxing conditions<sup>[73]</sup>. Rh110 can be easily prepared by removing 4 ethyl groups from RhB. Therefore RhB de-ethylation would have easily solved the problem. However de-ethylation of aromatic amines is difficult due to the strong C-N bond energy which is difficult to cleave without harsh conditions. The von Braun<sup>[74]</sup> reaction is the only known organic reaction to carryout N-dealkylation in which a tertiary amine reacts with cyanogen bromide to yield an organocyanamide. If such a procedure were available, Rh110 could have been easily obtained. In the first reports of Rh110, it was modified in order to synthesise fluorogenic amide substrates for assays of serine proteases<sup>[75–77]</sup> and caspases<sup>[78–80]</sup>.

Rh110 emerged as an excellent candidate since it is highly fluorescent as well as the uncleaved substrate is non-fluorescent (low background signal), and it is a perfect leaving group because cleavage of the amide bond is accompanied by a significant increase in the extent of aromatic conjugation (and thus a large increase in stability). Hence, several bis-substituted peptide<sup>[78–80]</sup> derivatives of Rh110 were synthesised and used in enzymatic activity studies. After this pioneering work in the synthesis of pro-fluorophore compounds, several bis-substituted peptide derivatives of Rh110 began to be traded by some chemical suppliers such as Aldrich or Molecular Probes. It can be seen in the Table 2.1 the cost of Rh110 to almost ~300 times as compared to RhB due to its

unique applications. The cost of commercial<sup>[81]</sup> Rhodamine dyes on average for common suppliers: Acros Organics, Aldrich, Alfa Aesar, Fluka, Radiant dyes laser, Sigma-Aldrich are provided in Table 2.1.

**Table 2.1-** Commercial Cost of common Rhodamine Dyes

Rhodamine Dye	Structure	Cost €/g
Rhodamine B		0.45
Rhodamine 110		128
Rhodamine 6G		1.60
Rhodamine 123		1650
Rhodamine 116		205

Rhodamine 101		80
Rhodamine 19		156

It is interesting that even though deethylation is not possible as a synthetic procedure, degradation of RhB via deethylation mechanism is long known, first observed by Honda<sup>[82]</sup> in 1977. Here we report a new catalyst with highly efficient deethylation ability; this is because the decomposition rate of the deethylated product is slow as compared to RhB. The yield is ~ 40% at pH=7 and is pH dependent.

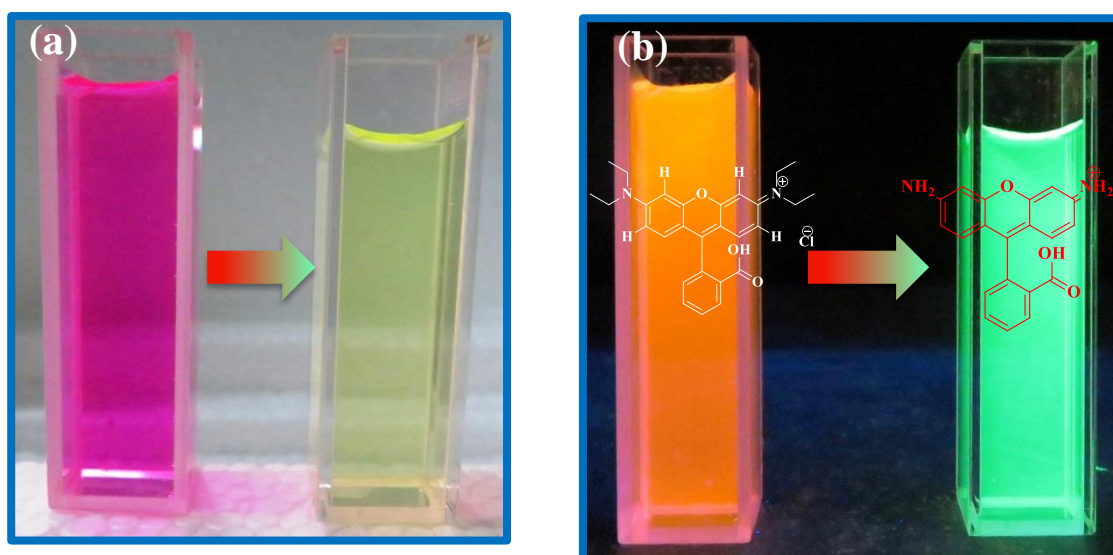


**Photo 2.1-** RhB converted to Rh110 after 130 min photoirradiation (a) in normal light; (b) under UV chamber

## 2.2 Photocatalytic dye degradation by metal loaded $\text{Bi}_4\text{TaO}_8\text{Br}$

The use of semiconductor materials for visible light assisted photocatalysis has developed as an exciting area of research to address the energy crisis issues related to sustainable fuel production and environmental remediation<sup>[83–86]</sup>. Moreover, semiconductor photocatalysts will have wide-ranging applications including, water disinfection<sup>[87]</sup> and organic pollutant degradation<sup>[88]</sup>. In dealing with organic pollutants, especially dyes, removal or degradation may be achieved by adsorption, complete breakdown or converting them into non-toxic fragments. To attain these goals by photocatalysis with efficient use of sunlight can pave the way for a cleaner and sustainable environment.

The discovery by Fujishima<sup>[26]</sup> and Honda in 1972 in their seminal paper on water splitting reaction for hydrogen generation using  $\text{TiO}_2$  as a semiconductor photocatalyst, However, its major drawback has been its high band gap of  $\sim 3.2$  eV, leading to inefficient absorption of sunlight (only  $\sim 4\%$  in the UV region). The research thrust has been extensively been carried out to find catalyst active under visible region<sup>[89–93]</sup>. In this regard, significantly promising advancements have been made on oxide semiconductors with layered structures. Notably, among them, Bi-containing layered oxides have drawn considerable attention due to their effective visible light absorption and high stability. On the other hand, it has been reported that the bandwidth originating from hybridization of Bi-6s with O-2p in these compounds is favourable for high carrier mobility leading to enhanced photocatalytic activity.

Recently, Bi-based compounds<sup>[94–96]</sup>, such as  $\text{BiOCl}$ <sup>[97]</sup>,  $\text{BiOBr}$ <sup>[98]</sup>,  $\text{BiOI}$ <sup>[99]</sup>,  $\text{BiOBr}_{1-x}\text{I}_x$ <sup>[100]</sup>, and  $\text{BiOI}_x\text{Cl}_{1-x}$ <sup>[101]</sup> has received considerable interest because of their enhanced catalytic activity under visible-light irradiation. Also, Tantalum and Bi-containing photocatalyst exhibited visible-light response ability such as.,  $\text{Bi}_3\text{Nb}_x\text{Ta}_{1-x}\text{O}_7$ <sup>[102]</sup>,  $\text{BiTaO}_4$ <sup>[103]</sup>, and  $\text{In}_2\text{TaO}_5$ <sup>[104]</sup>. The primary reason for such excellent efficiency can be attributed due to the internal electric fields in layered materials which favours charge separation, which subsequently induces redox reactions on the semiconductor surface and contribute towards photocatalytic activity<sup>[105,106]</sup>. In addition, the polarising fields existed between the distorted  $[\text{MO}_6]$  and  $[\text{BiO}_8]$  and existence of the interlayer permanent electric field hasten the separation of excitons upon photoirradiation, facilitating the high photocatalytic efficacy of layered materials.



The noble metal loaded semiconductor oxide systems demonstrates decreased recombination rates of excitons due to increased charge separation between the electrons and holes, in which the electrons gather on the metal and holes remain on surface of the photocatalyst. Though, metal loading onto a catalyst enhances photocatalytic activity, there are many instances in the literature where results are not always positive<sup>[107–109]</sup>, due to the oxidation states of the noble metals and also on the Fermi energy level. For example, Sano<sup>[110]</sup> *et al.* found that oxidized Pt, compared with metallic Pt exhibited a low improvement in the gas phase photodegradation of acetaldehyde. They attributed the advantage by metallic Pt over oxidized Pt owing to its ability to generate superoxide radical anions ( $O_2^{\cdot-}$ ). Very recently, Sillen- Aurivillius phases composed of Bismuth Niobium oxyhalide-  $Bi_4NbO_8Cl$ <sup>[111]</sup> has demonstrated excellent photocatalytic activity and stability in terms of photocatalytic water oxidation reactions. This phases are composed of two-layered phases, namely Sillen and Aurivillius represented as:  $[Bi_2O_2][A_{n-1}B_nO_{3n+1}][Bi_2O_2][X]_m$  ( $n = 1, m = 1, A = Pb^{2+}, Sr^{2+}; B = Nb, Ta, X = Cl, Br, I$  etc.). These oxyhalides have been earlier extensively investigated as multiferroics<sup>[112]</sup> and dielectrics<sup>[113]</sup>.

Motivated by these facts, we are interested in the further improvement of the photocatalytic activity of the layered bismuth tantalum oxyhalide perovskite. In this work, metal loaded (Pd, Pt, Ag) layered Bi-based oxyhalide  $Bi_4TaO_8Br$  ( $X = Cl, Br, I$ ) photocatalysts were synthesised, characterised, and used to degrade RhB dye in water. The photocatalytic activity of these catalysts was studied under visible light irradiation. Moreover, the observed photocatalytic activity follows the order  $Pd@Bi_4TaO_8Br > Pt@Bi_4TaO_8Br > Ag@Bi_4TaO_8Br > Bi_4TaO_8Br$ .

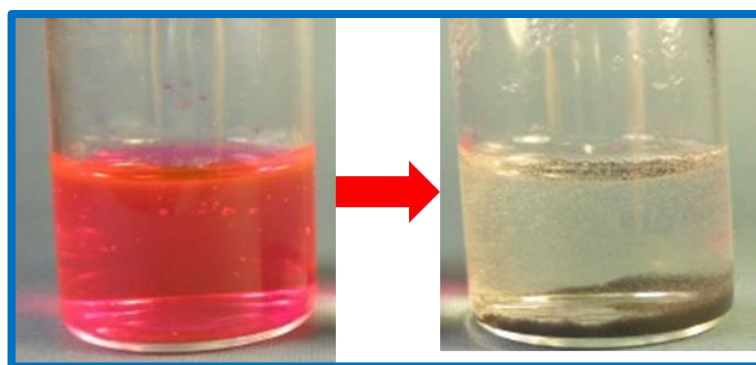


**Photo 2.2-** Photocatalytic degradation of RhB solution by prepared catalysts.

### 3. EXPERIMENTAL SECTION

#### Chemicals

Bismuth(III) Oxide ( $\text{Bi}_2\text{O}_3$ , HIMEDIA, 99.99%), Tantalum(V) Chloride ( $\text{Ta}_2\text{O}_5$ , Sigma Aldrich, 99.9%), Bismuth(III) nitrate Pentahydrate ( $\text{Bi}(\text{NO}_3)_3 \cdot 5\text{H}_2\text{O}$ , Sigma Aldrich, 99.99%), Potassium Chloride (KCl, HIMEDIA, 98%), Potassium Bromide (KBr HIMEDIA, 98%), Sodium Iodide (NaI, HIMEDIA, 98%), Palladium(II) Chloride ( $\text{PdCl}_2$ , Sigma-Aldrich, 99.99%), Silver Nitrate ( $\text{AgNO}_3$ , Sigma-Aldrich, 99.99%), Hexachloroplatinic acid Hexahydrate ( $\text{H}_2\text{PtCl}_6 \cdot 6\text{H}_2\text{O}$ , Sigma-Aldrich, 99.999%), Titanium(IV) Dioxide (P25  $\text{TiO}_2$ , Sigma Aldrich,  $\geq 99.5\%$ ), Rhodamine B ( $\text{C}_{28}\text{H}_{31}\text{ClN}_2\text{O}_3$ , Sigma Aldrich, 90%), Rhodamine 110 chloride ( $\text{C}_{20}\text{H}_{14}\text{N}_2\text{O}_3 \cdot \text{HCl}$ , Sigma Aldrich, 80%), Ethylene Glycol ( $\text{C}_2\text{H}_6\text{O}_2$ , Spectrochem, AR), Absolute ethanol ( $\text{C}_2\text{H}_5\text{OH}$ , Merck, 99.9%), Acetone ( $\text{C}_3\text{H}_6\text{O}$ , Rankem LR), Isopropanol ( $\text{C}_3\text{H}_8\text{O}$ , Merck, 99%) Potassium Bromide (KBr, IR Spectroscopy grade, HIMEDIA), Perchloric Acid ( $\text{HClO}_4$ , HIMEDIA), Tertiary butanol ( $\text{C}_4\text{H}_{10}\text{O}$ , Spectrochem, AR), Benzoquinone ( $\text{C}_6\text{H}_4\text{O}_2$ , Merck, AR), Ammonium Oxalate ( $\text{C}_2\text{H}_8\text{N}_2\text{O}_4$ , HIMEDIA, AR) and Sodium Hydroxide (NaOH, Rankem, AR) were used as received without further purification. Milli-Q water was used in all the experiments as required having resistance  $18.2 \text{ M}\Omega \text{ cm}^{-1}$ .

#### Synthesis of Bismuth Oxyhalide $\text{BiOX}$ (X= Cl, Br, I) Microspheres

The  $\text{BiOX}$  powders were synthesised by a simple soft chemical method<sup>[99]</sup>. In a typical synthesis,  $\text{Bi}(\text{NO}_3)_3 \cdot 5\text{H}_2\text{O}$  was added slowly into an EG solution containing stoichiometric amounts of KCl, KBr and NaI respectively, with the Bi to X molar ratio of 1. The mixture was stirred for 30 minutes at room temperature in air and then poured into a 25 mL Teflon-lined stainless autoclave until 80% of the volume was filled. The autoclave was then heated at 433 K for 12 hours under autogenous pressure, and then air cooled to room temperature. The resulting precipitates were collected and washed with ethanol and DI water thoroughly and dried at 323 K in air.

The mechanism for the formation of the hierarchical microspheres can be illustrated in the following three points:

1. Firstly, the formation of BiOX nanoparticles takes place and then they grow into nanoplates at the early stage of the formation.
2. Then, the solvent ethylene glycol induces the formation of self-assembly of these nanoplates to form loose microspheres
3. Lastly, the formation of hierarchical microspheres through a dissolution re-crystallisation process of the pre-formed nanoparticles takes place similar to Ostwald ripening.

The detailed illustration of the synthesis procedure and the formation mechanism of BiOX in via solvothermal process are provided below in Figure 2.1 and 2.2 respectively.

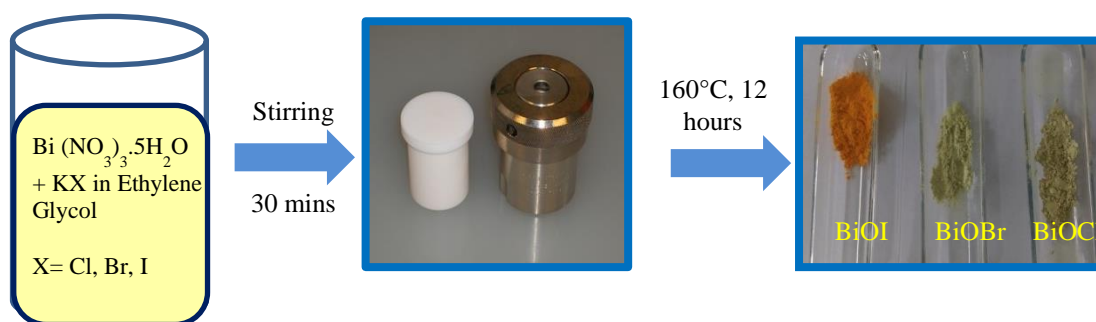


**Photo 3.1-** Schematic illustration showing solvothermal synthesis of BiOX.

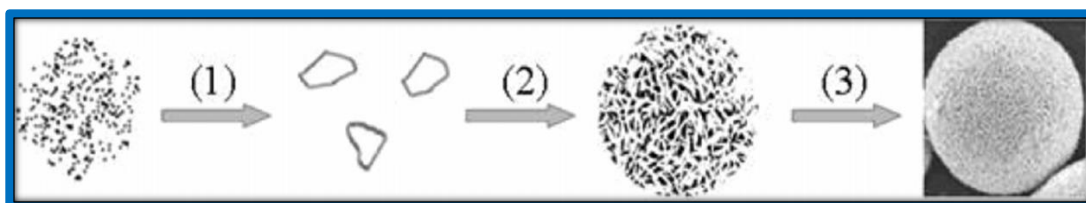


**Fig 3.2-** Illustration of the formation mechanism of hierarchical BiOX Microspheres<sup>[99]</sup>.

### Synthesis of Sillen-Aurivillius perovskite halide $\text{Bi}_4\text{TaO}_8\text{X}$

Stoichiometric quantities of  $\text{Bi}_2\text{O}_3$ , BiOX and  $\text{Ta}_2\text{O}_5$  powders were weighed, and then properly grounded in using mortar and pestle (Agate), and then the resulting powder was transferred in silica boat. After that, the boats were placed in a muffle furnace at 1073 K for 24 hours with intermediate grindings after 12 hours. The heating rate was 279 K per minute, and then naturally cooled to room temperature. The detailed illustration of the synthesis procedure is provided in Figure 2.3.



**Photo 3.3-** Schematic illustration of the synthesis of  $Bi_4TaO_8X$  via solid-state route.

### Synthesis of co-catalyst loaded $Bi_4TaO_8Br$

The metal nanoparticles loaded  $Bi_4TaO_8Br$  catalysts with less than 1 wt% were synthesized by photodeposition method under sunlight. Aqueous solutions of  $PdCl_2$ ,  $AgNO_3$ ,  $H_2PtCl_6 \cdot 6H_2O$  were weighed and put into 10 vol% aqueous methanol solutions in three beakers, to each of them 0.4 g of  $Bi_4TaO_8Br$  was added. The solutions were irradiated with 400W Xe light (Newport, USA) having a water filter (IR cutoff). The solution was purged with argon before starting the photodeposition, and after deposition, the solution was washed thoroughly with water-ethanol mixture and dried in air.

### Characterization

Powder X-ray diffraction (XRD) patterns were collected on a Rigaku Ultima IV diffractometer equipped with a 3 kW sealed tube  $Cu K\alpha$  X-ray radiation (40 kV and 40 mA) equipped with a DTex Ultra detector using parallel beam geometry ( $2.5^\circ$  primary and secondary solar slits,  $0.5^\circ$  divergence slit with 10 mm height limit slit). The samples were grounded into a fine powder using a mortar and a pestle was placed on a glass sample holder for room temperature measurement. The data were collected over  $2\theta$  from  $5^\circ$  to  $70^\circ$  with a scanning speed of  $2^\circ$  per minute with  $0.01^\circ$  step. Scanning electron microscopy (SEM) images were obtained using a field-emission scanning electron microscope (FESEM, JEOL, JSM-7600F).

The FE-SEM was operated with an accelerating voltage of 20-30 kV and a chamber pressure of  $10^{-5}$  Torr. All SEM samples were prepared by drop casting ethanolic solutions of the sample on silicon wafers and allowing the solvent to evaporate slowly at room temperature in a vacuum desiccator. The chemical composition of the prepared materials were measured by EDS (Energy Dispersive X-ray Spectroscopy, Oxford Instruments) operating at 10 kV.

The diffuse reflectance spectra (DRS) were measured using UV-vis spectrophotometer (Cary Series) and  $\text{BaSO}_4$  powder was used as the reference. The samples were grounded into a fine powder using a mortar and a pestle, and then transferred carefully into the solid holder maintaining uniformity of the surface. Photoluminescence Spectroscopy (PL) studies were carried using Spectrofluorometer (Horiba Scientific) using a quartz cuvette. All Time-Correlated Single Photon Counting (TCSPC) measurements were carried out in a Fluorocube, Horiba Jobin Yvon, NJ. For fluorescence lifetime measurements, the peak count was fixed to 10,000 and the excitation and emission polarizers were oriented at the magic angle ( $54.71^\circ$ ). For time-resolved fluorescence lifetime measurements, the peak difference was 10,000 counts and the orientation of the emission polarizer was  $0^\circ$  and  $90^\circ$  with respect to the excitation polarizer for parallel fluorescence intensities and perpendicular fluorescence intensities respectively. The emission monochromator for Rhodamine B and Rhodamine 110 was fixed at 583 nm and 533 nm respectively with a bandpass of 4 nm. The 375 nm laser diode was used as a light source for the excitation of both Rhodamine B and 110. The instrument response function (IRF) was collected using Ludox (colloidal silica). The width (FWHM) of IRF was  $\sim 250$  ps.

The flat-band potential was calculated using an electrochemical workstation (CHI-760 series, USA) using a conventional three-electrode cell. The 5mg catalyst was on a ITO with nafion, iso-propanol and water mixture (50 $\mu\text{l}$ :1ml:4ml) which served as the working electrode. Subsequently, Pt counter and a saturated Ag/AgCl reference electrode were used. AC amplitude and frequency were 10 mV and 1 kHz, respectively.

Fourier Transform Infrared Spectroscopy (FTIR) studies were carried on a Perkin Elmer Spectrum Two Spectrometer. Samples were grounded with KBr powder using a mortar and a pestle, and then the mixture was pressed into a pellet using a hydraulic press for further measurements. UV-Visible absorption spectroscopy studies were recorded using a Carry Series UV-Vis spectrophotometer at room temperature, the range of the measurement was from 200-800 nm with a step of 1nm.

The HRMS (Waters Synapt G2-Si Q-TOF Mass Spectrometer) studies were carried out in Electron Spray Ionization (ESI) mode with a Q-TOF Mass Analyser.

### **Photo-reactor and light source**

A 400 W Xe lamp was used as the visible light source with IR filter. A cut-off filter of 420nm was used to ensure only visible light can pass. The reactor used for the experiment is made of a pyrex glass beaker of volume 50 mL. In the reactor, 25 ml of solution was poured and continuously stirred to keep the suspension of catalyst uniform throughout the solution.

### **Photocatalytic Experiments**

An aqueous 25 mL dye solution with a concentration of 10 mg/L of dye was used for all photocatalytic studies. The amount of catalyst used was fixed as 40 mg for 25 ml of dye solution, unless otherwise mentioned. The suspension containing dye solution and catalyst was magnetically stirred for 30 minutes in the dark to attain adsorption-desorption equilibrium and the resulting aliquot was exposed to light for photo-conversion.

Photocatalytic experiments were carried out under visible light irradiation using the above mentioned light source. Temperature dependent and pH dependent reaction was also carried out. The solution pH was adjusted using HClO<sub>4</sub> and NaOH. During the illumination of the light, 1 ml of solution was continuously taken from the reaction cell for regular intervals of time. The collected samples were then centrifuged to remove any catalyst particle present in the solution for further analysis. Dye solutions were analysed based on Beer-Lambert law at its maximum absorption wavelength.

## 4. RESULTS AND DISCUSSION

### 4.1 Photocatalytic transformation of Rhodamine B to Rhodamine 110

#### 4.1.1 Powder X-ray Diffraction

The Powder X-ray diffraction patterns showed that the prepared tetragonal BiOX and orthorhombic Bi<sub>4</sub>TaO<sub>8</sub>X are single phase as shown in the Figure 4.1 and 4.2. The average crystal size of the samples is estimated to be about 2 μm by the Debye-Scherrer equation,

$$D = \frac{0.89\lambda}{\beta \cos \theta}$$

(where D is the crystallite size in nm, λ is the Cu Kα wavelength, β is the half-width of the peak in radians, and θ is the corresponding diffraction angle). The lattice parameters and average crystallite size of the prepared Bi<sub>4</sub>TaO<sub>8</sub>X are mentioned in the Table 4.1.

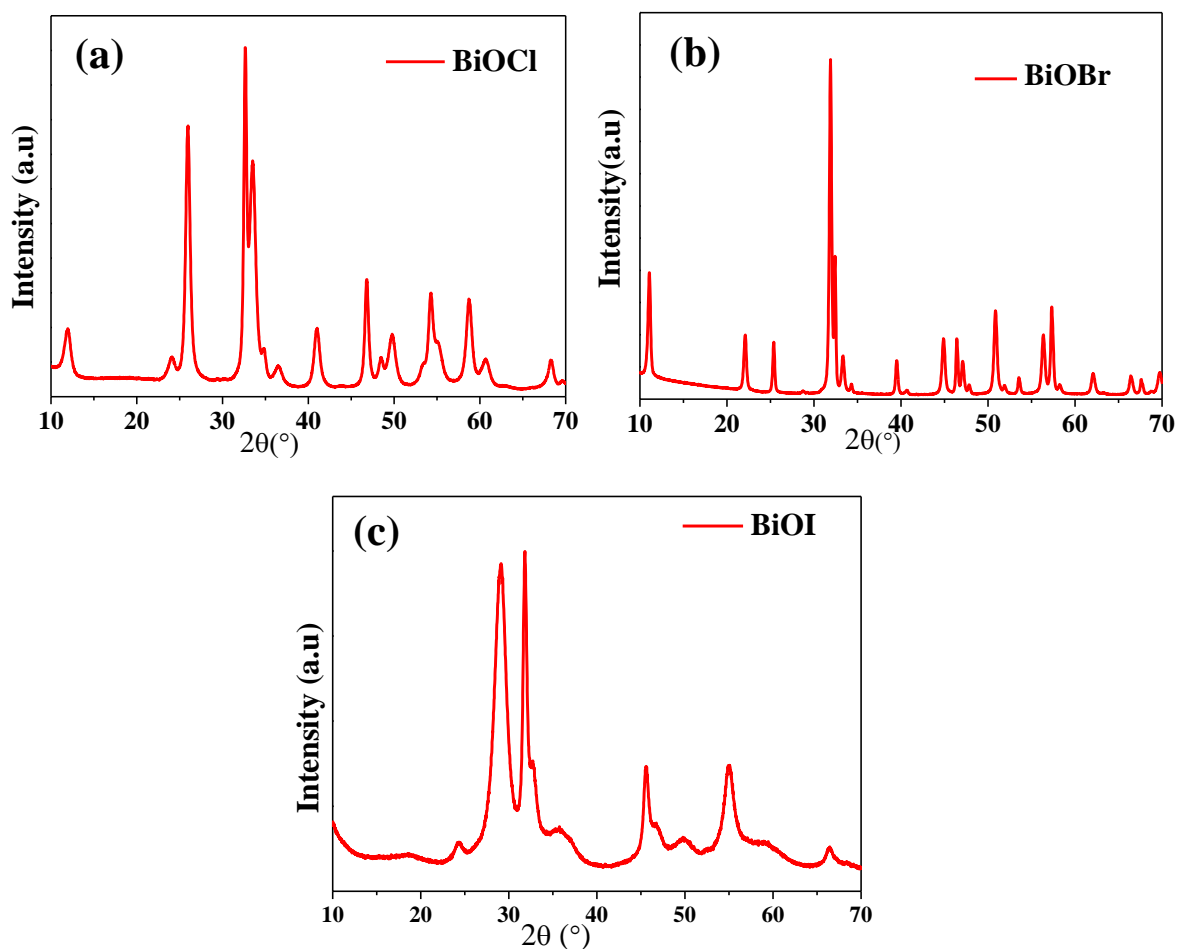
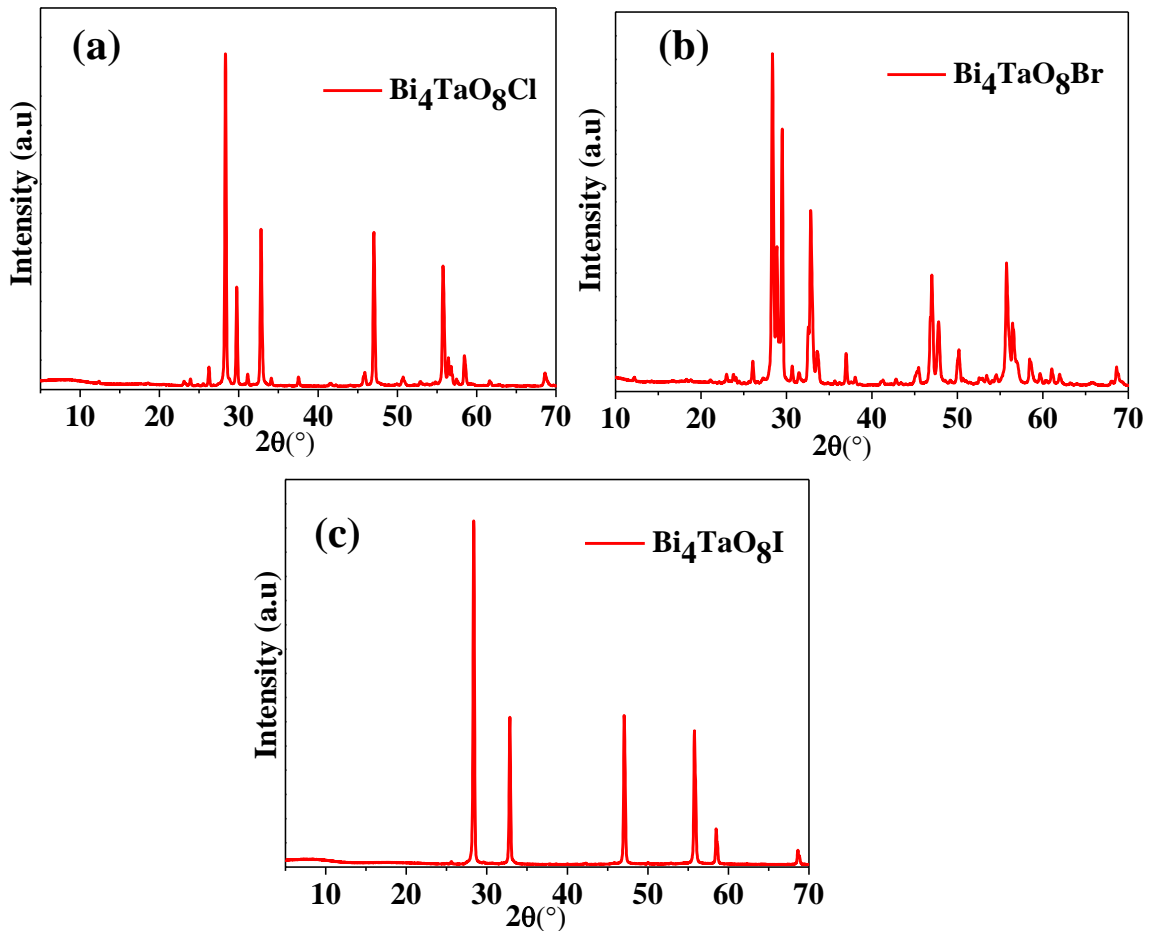


Fig 4.1- PXRD patterns of (a) BiOCl, (b) BiOBr and (c) BiOI.



**Fig 4.2-** PXRD patterns of (a)  $\text{Bi}_4\text{TaO}_8\text{Cl}$ , (b)  $\text{Bi}_4\text{TaO}_8\text{Br}$  and (c)  $\text{Bi}_4\text{TaO}_8\text{I}$ .

**Table 4.1-** Table of lattice parameters of  $\text{Bi}_4\text{TaO}_8\text{X}$

Catalysts	$\text{Bi}_4\text{TaO}_8\text{Cl}$	$\text{Bi}_4\text{TaO}_8\text{Br}$	$\text{Bi}_4\text{TaO}_8\text{I}$
<b>a</b> (Å)	5.4770	5.4942	5.5279
<b>b</b> (Å)	5.5166	5.5356	5.5656
<b>c</b> (Å)	28.5658	29.0375	29.5001
<b>Avg. Crystallite Size</b> (μm)	2.35-2.40	2.34-2.36	2.32-2.39

#### 4.1.2 Field Emission Scanning Electron Microscopy

The morphology and size of the samples were characterized by field emission scanning electron microscopy (FE-SEM). Figure 4.3, shows the microspheres of  $\text{BiOX}$ ,



with sizes of 250-150nm obtained readily by the solvothermal method. Figure 4.3 exemplifies the SEM micrograph of  $\text{Bi}_4\text{TaO}_8\text{X}$  with average size  $\sim 2\ \mu\text{m}$ .

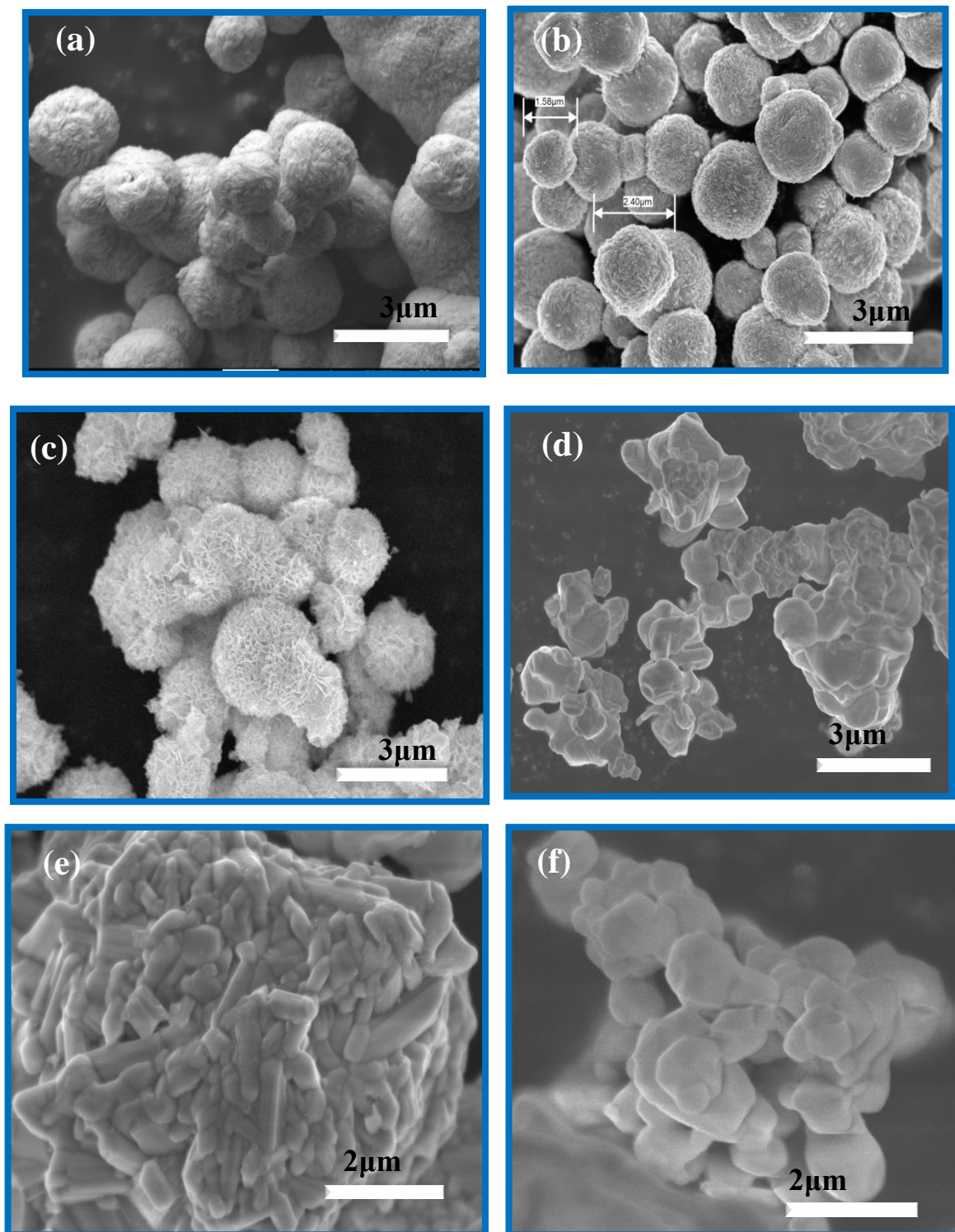


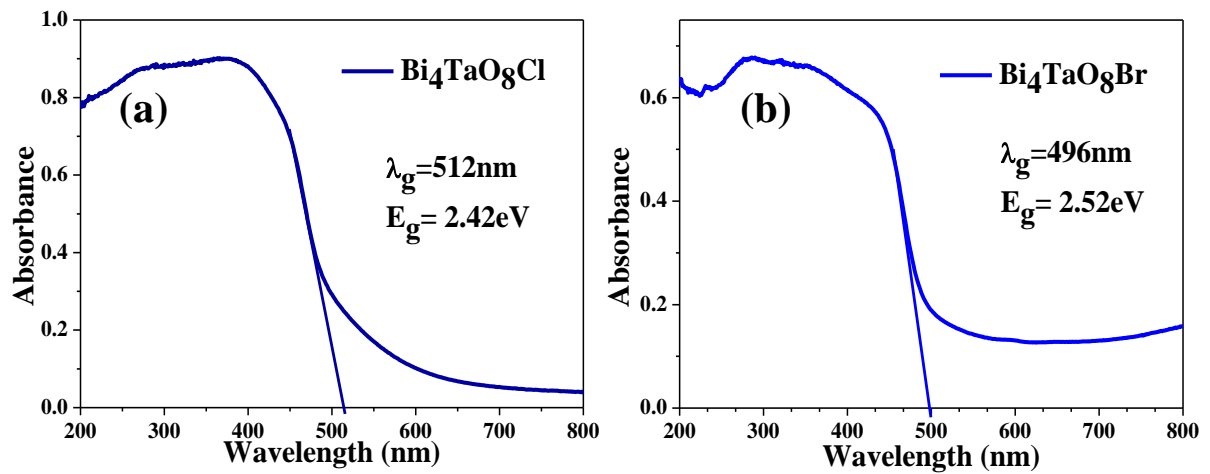
**Fig 4.3-** SEM images of (a)  $\text{BiOCl}$ , (b)  $\text{BiOBr}$ , (c)  $\text{BiOI}$ , (d)  $\text{Bi}_4\text{TaO}_8\text{Cl}$ , (e)  $\text{Bi}_4\text{TaO}_8\text{Br}$  and (f)  $\text{Bi}_4\text{TaO}_8\text{I}$ .

### 4.1.3 Diffuse Reflectance Spectroscopy (DRS)

UV-vis diffuse reflectance spectra (DRS) were obtained using a UV-Vis spectrometer by using BaSO<sub>4</sub> as a reference and were converted from reflection to absorbance by the Kubelka-Munk method. To calculate the optical band gap, the following Tauc<sup>[114]</sup> equation was used:

$$\alpha h\nu = A(h\nu - E_g)^{n/2}$$

(where A = constant,  $h\nu$  = light energy,  $E_g$  = optical band gap energy,  $\alpha$  = measured absorption coefficient) For in-direct band gap materials, in the equation, n reflects the characteristics of the transition in a semiconductor, i.e. n = 1 for direct transition and n = 4 for indirect transition, Bi<sub>4</sub>TaO<sub>8</sub>Br is known as an indirect semiconductor. In Figure 4.4, we show the optical absorption spectra of Bi<sub>4</sub>TaO<sub>8</sub>X in the orthorhombic structure. The perovskite show typical semiconductor absorption spectra with extended visible light absorption. It can be observed according to the spectrum, a steep absorption edge of the samples fall in the visible region of the spectrum. Absorption originates from the UV region and continues up to visible region which establishes that these materials are potential candidates to show photocatalytic activity in the visible region. The observed band gap is consistent with the intense yellow colour of n-type semiconductor Bi<sub>4</sub>TaO<sub>8</sub>X. The band gap is estimated to be 2.42 eV, 2.52 eV and 2.13 eV for Bi<sub>4</sub>TaO<sub>8</sub>Cl, Bi<sub>4</sub>TaO<sub>8</sub>Br and Bi<sub>4</sub>TaO<sub>8</sub>I respectively.



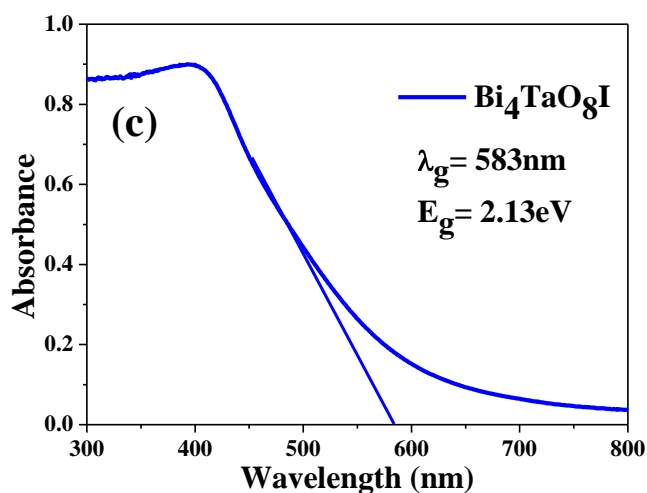


**Fig 4.4-** DRS plots of (a)  $\text{Bi}_4\text{TaO}_8\text{Cl}$ , (b)  $\text{Bi}_4\text{TaO}_8\text{Br}$  and (c)  $\text{Bi}_4\text{TaO}_8\text{I}$ .

#### 4.1.4 Crystal Structure of $\text{Bi}_4\text{TaO}_8\text{X}$

The Sillen-Aurivillius phase,  $\text{Bi}_4\text{MO}_8\text{X}$  is a layered structure that crystallizes in orthorhombic phase with  $\text{P2}_1\text{cn}$  space group and was first synthesised by John F. Ackerman<sup>[115]</sup>. As reported by Kusainova<sup>[116]</sup> *et al.*,  $\text{Bi}_2\text{O}_2$ ,  $\text{TaO}_4$  and Cl layers are stacked one over the other and forming a stable, unique layered intergrowth perovskite along c direction (Figure 4.5). The Sillen–Aurivillius phases are structurally very similar to the Aurivillius phases, but with an additional halide layer between the  $[\text{Bi}_2\text{O}_2]^{2+}$  layers. The series can be described as  $[\text{Bi}_2\text{O}_2] [\text{A}_{n-1}\text{B}_n\text{O}_{3n+1}] [\text{Bi}_2\text{O}_2] [\text{X}_m]$  where n is the number of perovskite layers (A), and m the number of halide layers (X); abbreviated to  $\text{A}_n\text{X}_m$ .

The corner sharing  $\text{TaO}_6$  octahedrons show a considerable degree of distortion and tilting in the crystal structure. Similar to  $\text{Bi}_4\text{NbO}_8\text{Cl}$ <sup>[94]</sup> structure, there are two coordination environments of Bi: distorted  $\text{BiO}_8$  and anti-square prism comprising of  $\text{BiO}_4\text{Cl}_4$  moiety. Induced polarization field between the  $\text{TaO}_6$  octahedra and  $\text{Bi}_2\text{O}_2$  layers, and between [Cl] and  $[\text{Bi}_2\text{O}_2]$  layers are believed to be responsible for effective electron–hole separation.

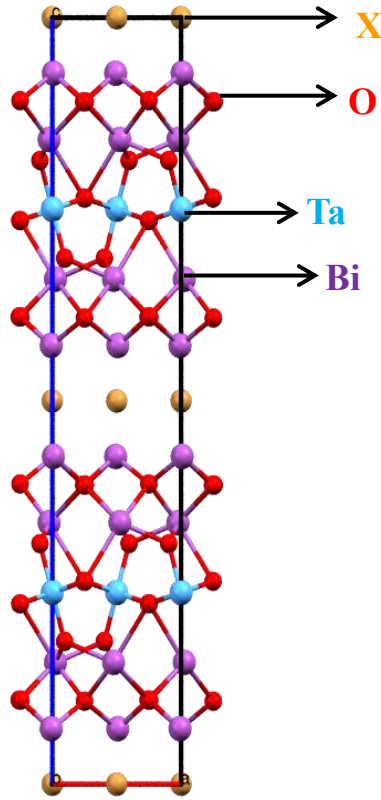


**Fig 4.5-** *Crystal Structure of  $\text{Bi}_4\text{TaO}_8\text{X}$  consisting of Sillen and Aurivillius blocks*

#### 4.1.5 Flat Band Potential

The flat-band potential of  $\text{Bi}_4\text{TaO}_8\text{Br}$  was determined from the Mott–Schottky<sup>[117]</sup> plot. The Mott–Schottky equation relates the capacitance to the applied voltage across a semiconductor-electrolyte junction.

$$\frac{1}{C_{SC}^2} = \frac{2}{\epsilon_0 \epsilon_r e N_A} \left( V_{applied} - V_{fb} - \frac{kT}{e} \right)$$

where,  $C_{SC}$  is a specific capacitance of our material;  $\epsilon_0$ ,  $\epsilon_r$ ,  $e$  and  $N_A$  are permittivity of vacuum, relative permittivity, electron charge and donor concentration respectively;  $V_{applied}$  and  $V_{fb}$  are applied potential and flat band potential of materials respectively;  $kT$  is a Boltzman energy term. In the above equation, the value  $\frac{(kT)}{e}$  is negligible, in comparison with the other term, hence the above equation takes the below form for present analysis.

$$\frac{1}{C_{sc}^2} = \frac{2}{\epsilon_o \epsilon_r e N_A} (V_{applied} - V_{fb})$$

We obtained the flat band potential in an aqueous 0.1 M Na<sub>2</sub>SO<sub>4</sub> solution (pH = 2) shown in Figure 4.6. We obtained -0.367 V (vs Ag/AgCl) corresponding to -0.24 V (vs SHE at pH = 2). Supposing that the flat-band potential is located just below conduction band minimum (CBM), the VBM (valence band maximum) has been estimated to be ~2.28 V using its band gap.

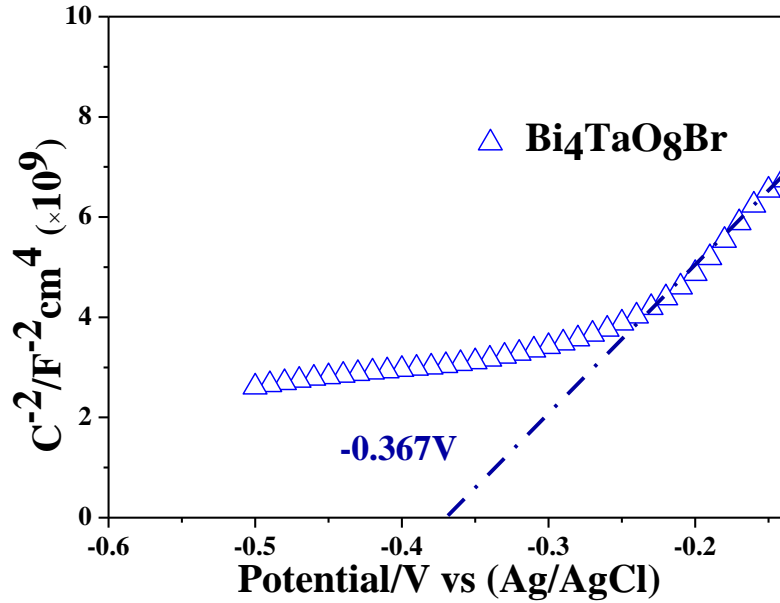


**Fig 4.6-** Mott-Schottky plot of Bi<sub>4</sub>TaO<sub>8</sub>Br in 0.1 M Na<sub>2</sub>SO<sub>4</sub> solution (pH=2).

#### 4.1.6 Visible light driven photocatalysis

Photocatalytic activity of Bi<sub>4</sub>TaO<sub>8</sub>Br has been investigated under visible light irradiation. Rhodamine B has been selected as a model dye for evaluation of the photocatalytic activity. Rhodamine B is a structurally stable cationic dye, which is represented in Figure 4.7. Rhodamine B (RhB, Mol. Wt.= 479.02,  $\lambda_{\text{max}}$ = 553 nm) also known as Basic Violet 10, is a xanthene dye with chemical formula C<sub>28</sub>H<sub>31</sub>ClN<sub>2</sub>O<sub>3</sub> (Colour Index No- 45170). The chemical name of Rhodamine B is [9-(2-carboxyphenyl)-6-diethylamino-3-xanthenylidene]-diethylammonium chloride, which is red in colour in aqueous solution. It is highly soluble in water (15 g/ L) and aromatic amines formed from the natural reductive anaerobic degradation of Rhodamine B are potential carcinogens<sup>[3]</sup>.

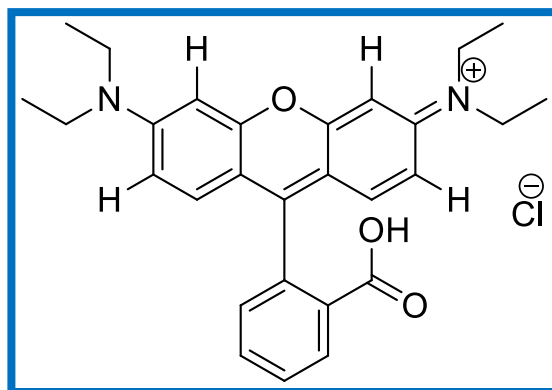


**Fig 4.7-** Chemical Structure of Rhodamine B

The spectral changes taking place during the photodegradation of RhB over  $\text{Bi}_4\text{TaO}_8\text{Br}$  is shown in Figure 4.8 at  $\text{pH}=7$ . RhB has its major absorption peak at 553 nm whose absorbance decreases with time under light irradiation. The RhB/ $\text{Bi}_4\text{TaO}_8\text{Br}$  aqueous dispersion undergone a decrease in absorption when irradiated with visible light ( $\lambda > 420$  nm) as shown in Figure 4.8. It also leads to a simultaneous wavelength shift of the band to shorter wavelengths. Under visible illumination, the dye is de-ethylated in a stepwise manner with the colour of the dispersion changing from an initial red colour to a light green with the ethyl groups are removed stepwise, as confirmed by the gradual peak wavelength shifts toward the blue region.

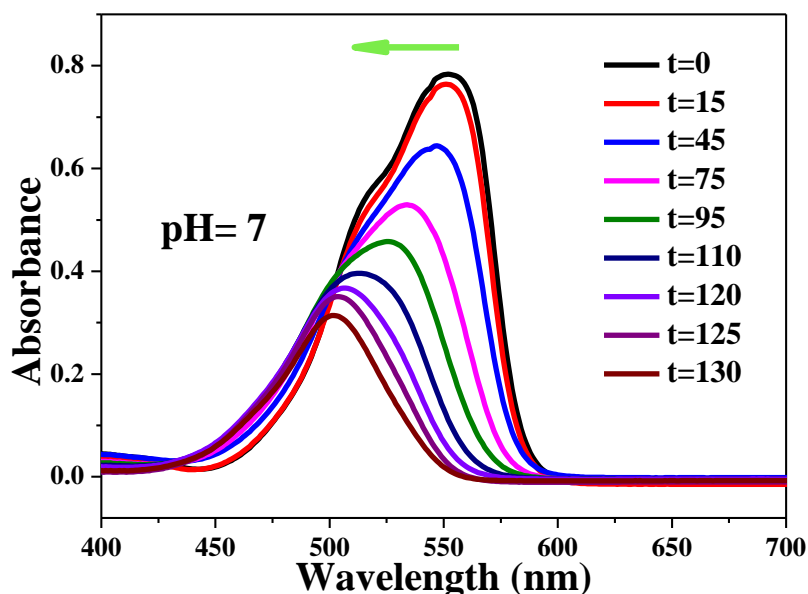


**Fig 4.8-** Temporal UV-Vis spectra of RhB conversion to Rh110 using  $\text{Bi}_4\text{TaO}_8\text{Br}$  under visible light irradiation.

The fully de-ethylated RhB molecule, i.e, Rh110 has its  $\lambda_{\max}$  at 500 nm. The observed blue shift is due to the N-dealkylation pathway as known in literature. For comparison similar photocatalytic conversion was done on RhB by  $\text{TiO}_2$  (P-25). We observed the loss of RhB over P-25 was faster as well as did not undergo a blue shift as in the case of  $\text{Bi}_4\text{TaO}_8\text{Br}$ . We carried out photocatalysis of Rhodamine B to Rh110 at different pH. Moreover, observed that with the increase in pH, the yield of the Rh110 increased to a maximum at pH=7 and then decreased beyond that. The observation can be attributed due to the differential adsorption of the dye on the catalyst surface with the change of pH. It has been known in the literature that Rhodamine B undergoes degradation by two pathways: 1. Chromophore Cleavage; 2. N-dealkylation. The photodegradation of RhB over  $\text{Bi}_4\text{TaO}_8\text{Br}$  with different initial pH was carried out, and the percentage yield is showed in Figure 4.9.

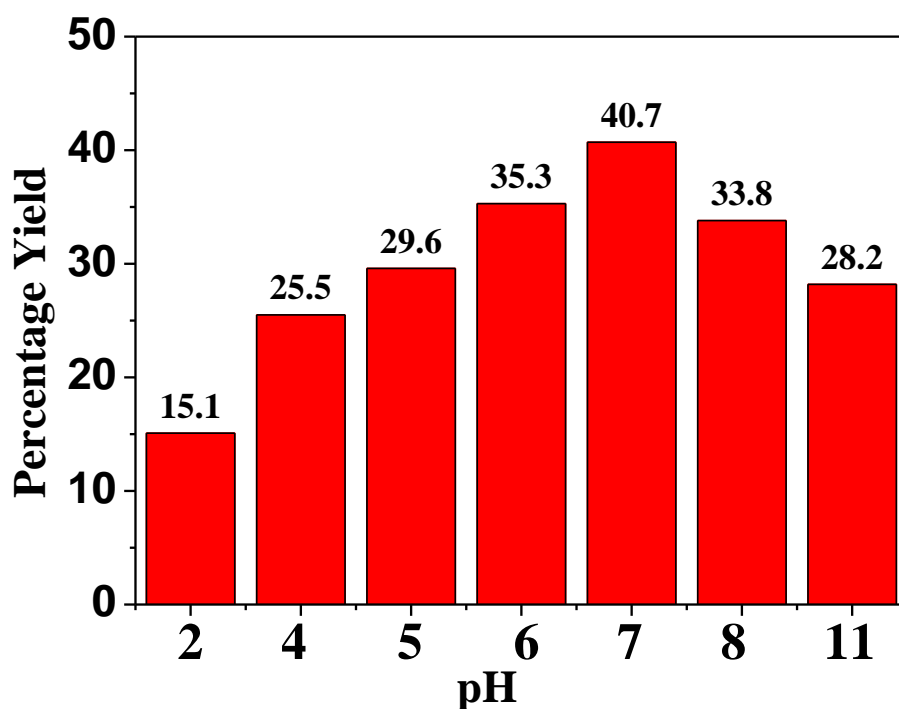


**Fig 4.9-** pH dependent percentage yield of RhB conversion to Rh110 using  $\text{Bi}_4\text{TaO}_8\text{Br}$

A variation in pH had a dramatic influence on the degradation of RhB in aqueous  $\text{Bi}_4\text{TaO}_8\text{Br}$  dispersions. The photoconversion rate of the RhB dye increased from pH 2 to 7 and decreased after that. Also, at pH=7 we get the maximum amount of N-dealkylated product. Comparing the UV-Visible absorption spectrum after 130 min of irradiation with that of starting shows that approximately 40% of RhB formed Rh110 after being fully dealkylated and the rest was degraded through the destruction of the conjugated structure.

The catalyst has a positive surface charge at lower  $pH$  which facilitates the adsorption of RhB through the lone pairs of amino groups present in RhB and undergoes faster degradation via chromophore cleavage as compared to N-dealkylation. The existing  $pH$  of the solutions can affect the magnitude of adsorption of RhB on the catalyst surface and thus may indirectly enhance the transformation rate of RhB. To further reveal the relationship between the extent of adsorption and the dealkylation process, we carried out the influence of  $pH$  on the adsorption of RhB on the catalyst surface, as shown in Figure 4.9. The initial rate of RhB conversion increased with an increase in the  $pH$  of the dispersion in the range from  $pH$  2-11, but decreased thereafter due to the adsorption of RhB by the catalyst promote the transformed rate.

Xanthene based dyes are known to show excellent fluorescence in the visible light, making it useful for various applications. We have also carried out the photoluminescence studies with time of the RhB/ $Bi_4TaO_8Br$  aqueous dispersion at  $pH=7$ . The temporal changes of the emission maxima were observed in photoluminescence spectrum shown in Figure 4.10.

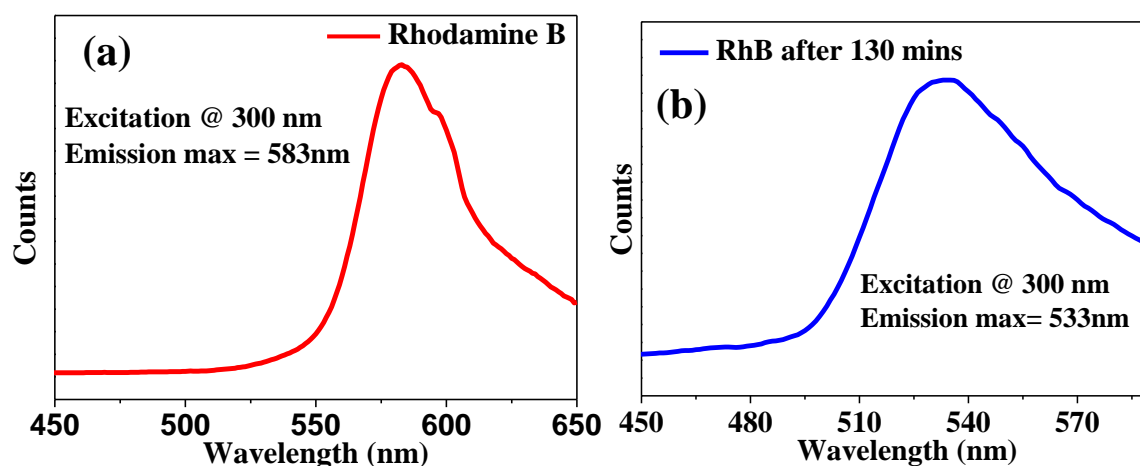


**Fig 4.10-** Photoluminescence spectras (a) before and (b) after photoirradiation

RhB dye is known to have its emission maxima at 583 nm in water, so with the passage of time, it has undergone a blue shift to 533 nm corresponding to the emission maxima of Rh110. The excitation was carried at 300 nm for all the PL spectras, so we see the second harmonic coming up in the spectrum at 600 nm. So, from the PL studies, it can be concluded that the catalyst-RhB aqueous dispersion in the presence of light gets converted to Rh110.



To identify the species produced in the photochemical conversion of RhB, the High Resolution Mass Spectrometry studies of the dye, intermediates, and final products were done as shown in Figure 4.11 and 4.12.

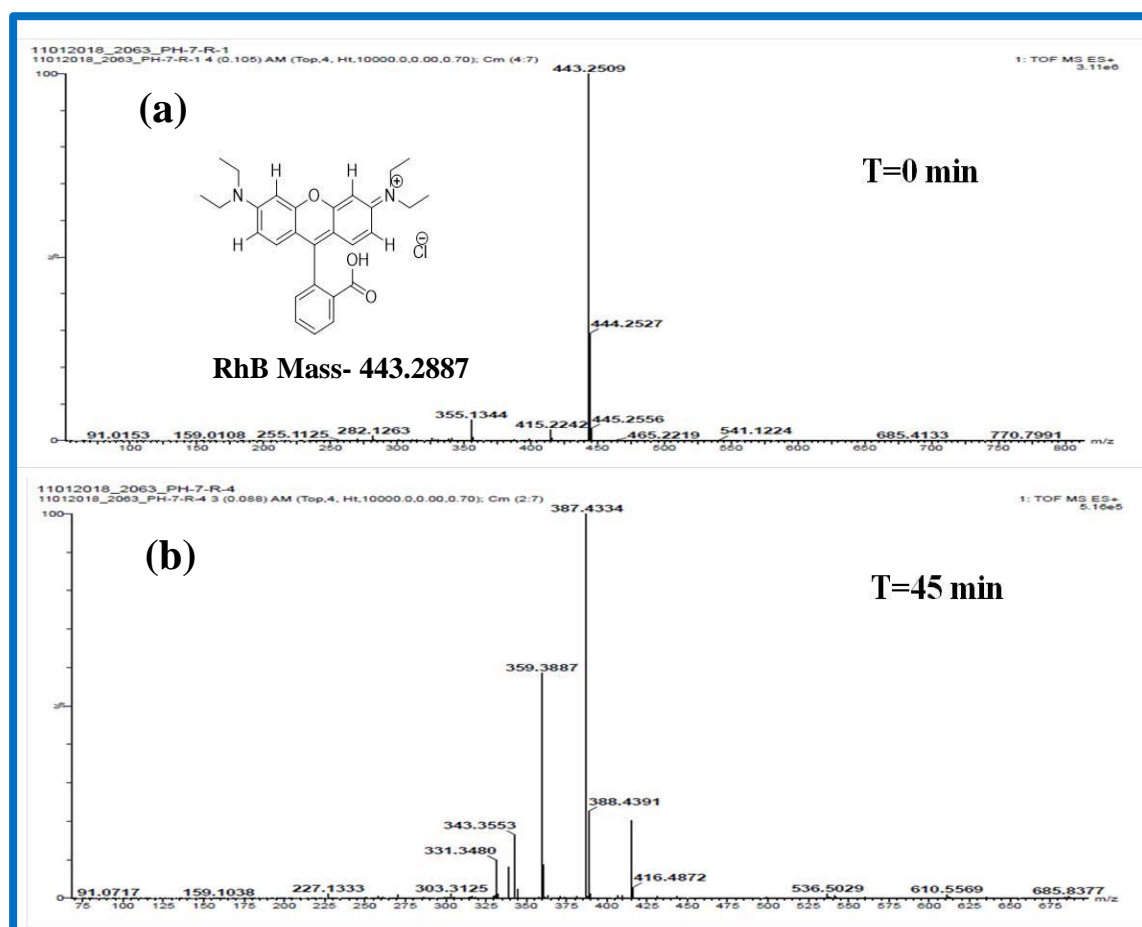


**Fig 4.11-** HRMS spectra collected at different intervals (a) 0 min (b) after 45 min photoirradiation.

The Rhodamine B has its characteristic molecular ion peak at 443 m/z, which undergoes stepwise converted to Rhodamine 110 having molecular ion 331 m/z. The change in the mass spectrometry was examined at specific time intervals of the photocatalysis. It was observed that 28 m/z fraction representing an ethyl group was deducted from the 443,418,387,359 and finally stopping at 331. So, the phenomenon of N-dealkylation could be monitored by HRMS at different time intervals, and we obtain pure Rh110. It is to be also noted that pure RhB contains an impurity at 355 m/z, but with the passage of time, we observe that the impurity vanishes after 75 mins of photoirradiation of RhB/Bi<sub>4</sub>TaO<sub>8</sub>Br.

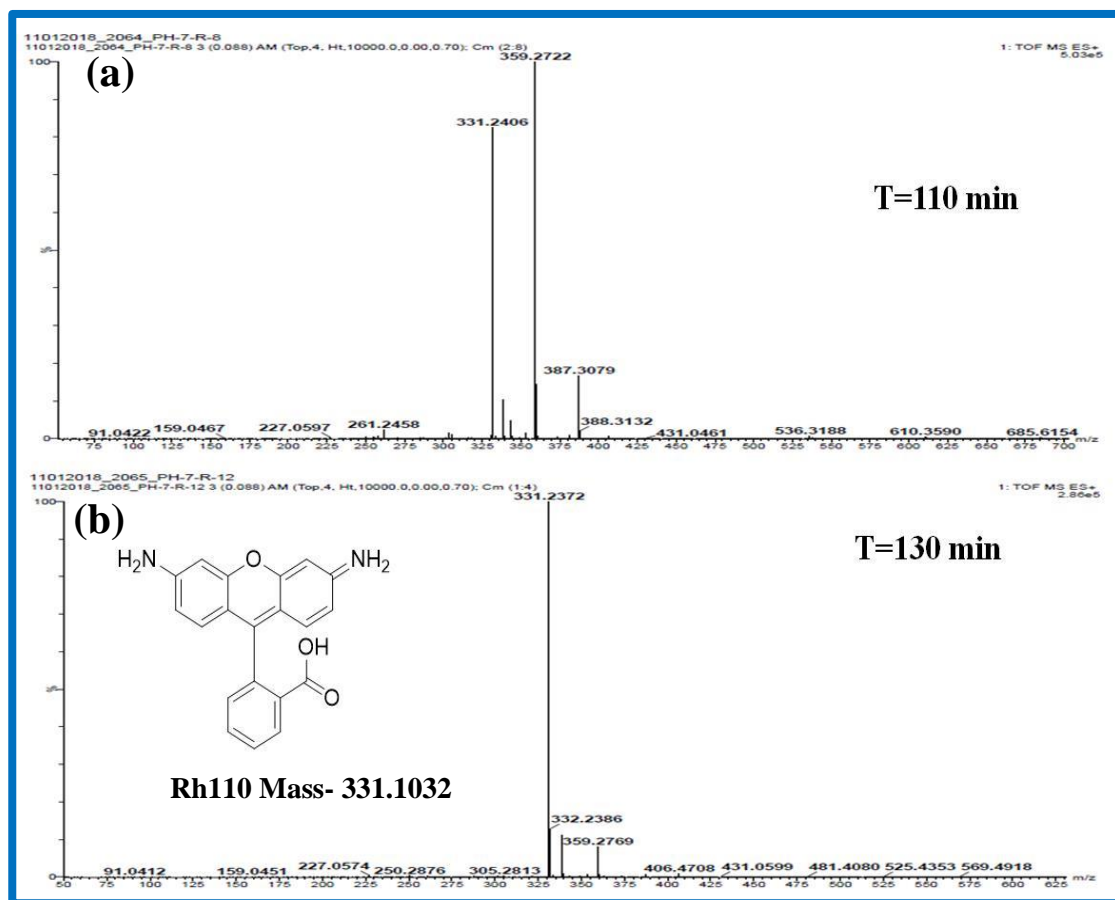


**Fig 4.12-** HRMS spectra collected at different intervals (a) 110 min (b) after 130 min photoirradiation.

We can carry on until 50 cycles with considering normal concentrations used for such investigations by other researchers. After 50 Cycles, we see only ~ 30% slowdown in the catalyst efficiency, but no change in the percentage of yield of Rh110 yield and remain nearly same. Numerically, we converted 25 mg of RhB (each cycle-0.25mg/20 mL) with 40 mg of catalyst and obtained about ~ 4 mg of Rh110. In all the papers, the investigation is limited to about 0.25 mg. Therefore we have demonstrated the excellent efficacy of the process to 50 repeat times as compared to state-of-the-art examples.

Further, we have found that the catalysis becomes slow when RhB concentration is about 200  $\mu\text{M}$  due to high absorption of light by the dye. Therefore we have done 50 equivalent cycles using 10 equivalent cycles at a time. We further used natural sunlight to examine our hypothesis, and observed similar efficiency as that of the simulated visible light, as shown in the Figure 4.13.

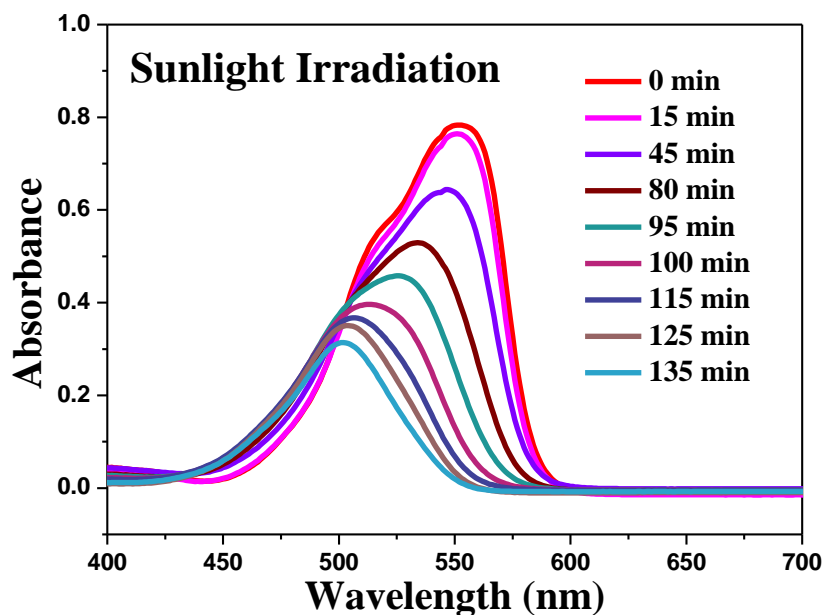


**Fig 4.13-** Temporal UV-Visible spectra of RhB conversion to Rh110 using  $\text{Bi}_4\text{TaO}_8\text{Br}$  under sunlight irradiation.

Moreover, we have found that the catalyst efficiency can be regained after 50 cycles by simple heating in air at 1023 K for 5 mins, as evident from the powder X-ray diffraction in Figure 4.14.

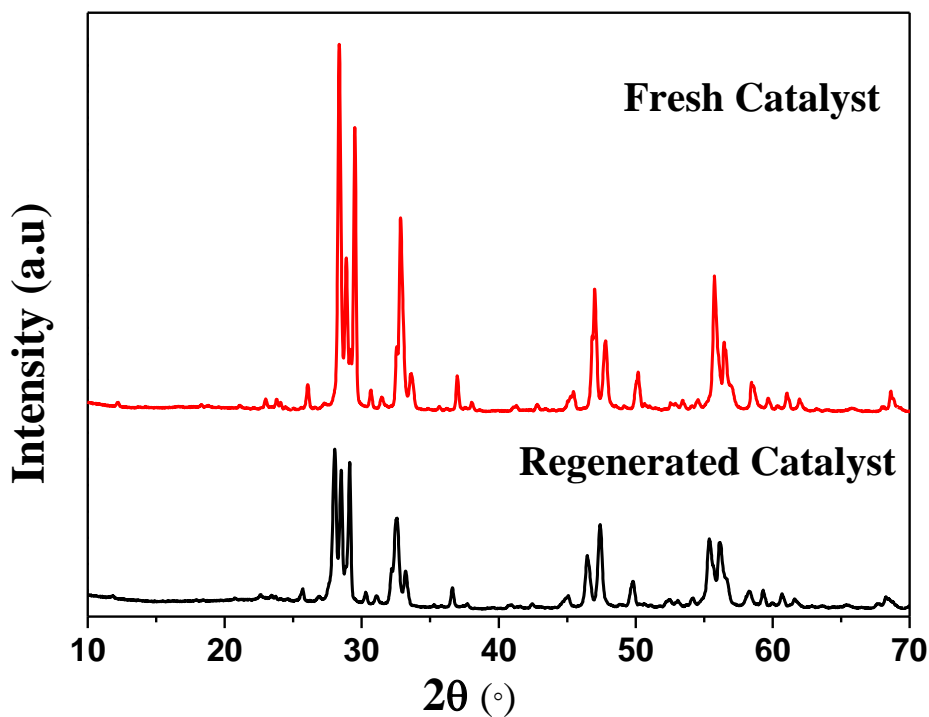


**Fig 4.14-** PXRD patterns of Fresh and Regenerated catalyst.

To understand the adsorption phenomenon of the dye over the catalyst surface, we carried out adsorption studies at a very lower concentration of RhB ( $5 \mu\text{M}$ ) in the dark for 24 hours and recording the UV-Visible spectra after regular intervals of time. Figure 4.15 illustrates the temporal UV-Visible spectra of the adsorption phenomenon which exemplifies that RhB adsorption on the catalyst surface is negligible for 2 hours, but it is significant once it has been kept for an elongated period of 24 hours. This study infers that the conversion of RhB to Rh110 takes place only in the presence of visible light.

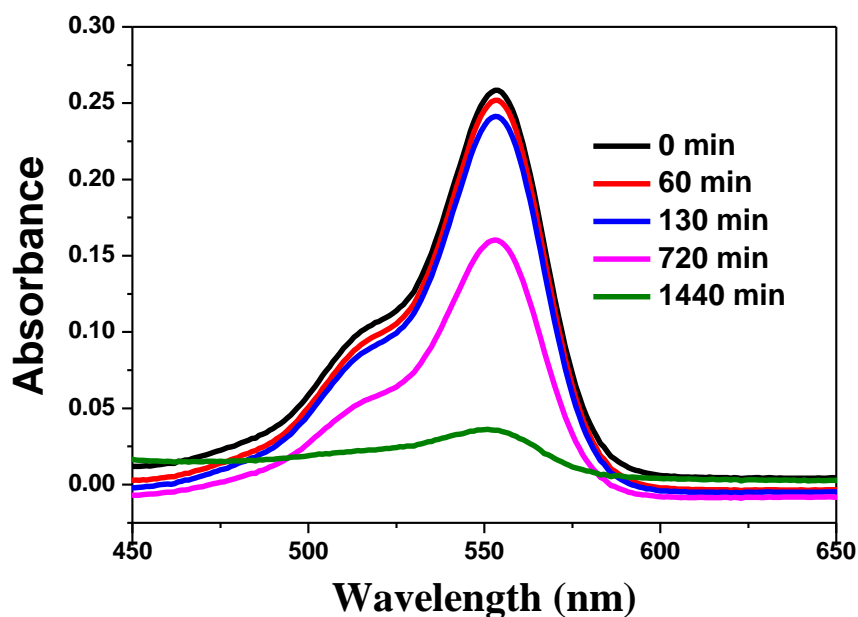


**Fig 4.15-** UV-Visible spectra of adsorption studies carried out till 24 hours

Also, FTIR spectra of RhB dye,  $\text{Bi}_4\text{TaO}_8\text{Br}$  and RhB adsorbed on  $\text{Bi}_4\text{TaO}_8\text{Br}$  (after photo irradiation) were recorded as shown in Figure 4.16. According to previous literature<sup>[118]</sup>, the assignments for the RhB (before irradiation) are as follows: the bands at  $3430 \text{ cm}^{-1}$  are due to  $-\text{OH}$  stretch vibration, the bands at  $2974, 2928 \text{ cm}^{-1}$  are caused by  $-\text{CH}_2-$  and  $\text{C}-\text{CH}_3$  stretch vibration, respectively. The peaks at  $1590, 1528, 1468 \text{ cm}^{-1}$  correspond to aromatic ring vibrations, while the  $1341 \text{ cm}^{-1}$  peak attributes to C-aryl bond vibration; the peak at  $1720 \text{ cm}^{-1}$  are due to  $\text{C}=\text{O}$  groups. The peak at  $1646 \text{ cm}^{-1}$  is caused by vibrations of the  $\text{C}-\text{N}$  bond and the heterocycle vibrations cause the peak ranging at  $1530-1558 \text{ cm}^{-1}$ . After the photoirradiation, the IR spectra of RhB adsorbed on the  $\text{Bi}_4\text{TaO}_8\text{Br}$  show that there is no RhB adsorbed on the surface of the catalyst as above evident peaks are not observed.

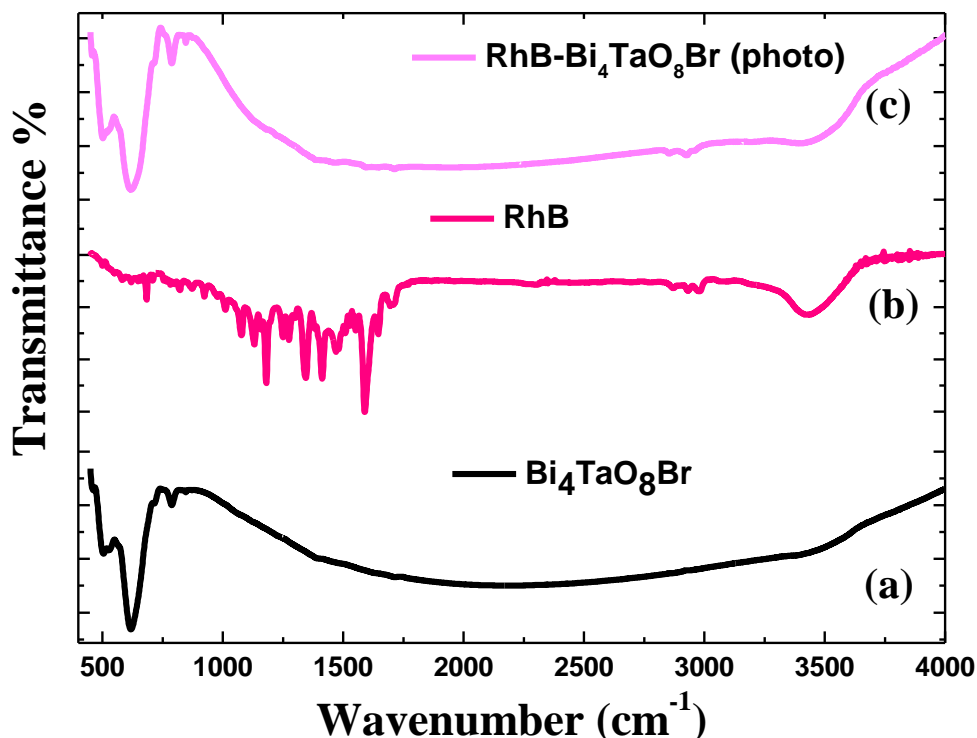


**Fig 4.16-** FTIR spectra (a)  $\text{Bi}_4\text{TaO}_8\text{Br}$  (b) Rh B (c) RhB- $\text{Bi}_4\text{TaO}_8\text{Br}$  after photoirradiation

Consequently, the fluorescence lifetime ( $\tau_1$ ) of RhB in aqueous solution was determined to be 1.75 ns, while a 3.85 ns lifetime ( $\tau_2$ ) of the de-ethylated RhB or Rh110 was obtained by fitting the trace after 130 min irradiation shown in Figure 4.17. According to  $I(t) = A_1 \exp(-t/\tau_1) + A_2 \exp(-t/\tau_2)$ , the traces were fitted by bi-exponentially. These parameters demonstrate that the amount of reactant RhB decreases while the produces Rh110 with a longer lifetime as the irradiation time goes on. The recorded lifetime of Rh110 is in agreement with that of the literature reported values.

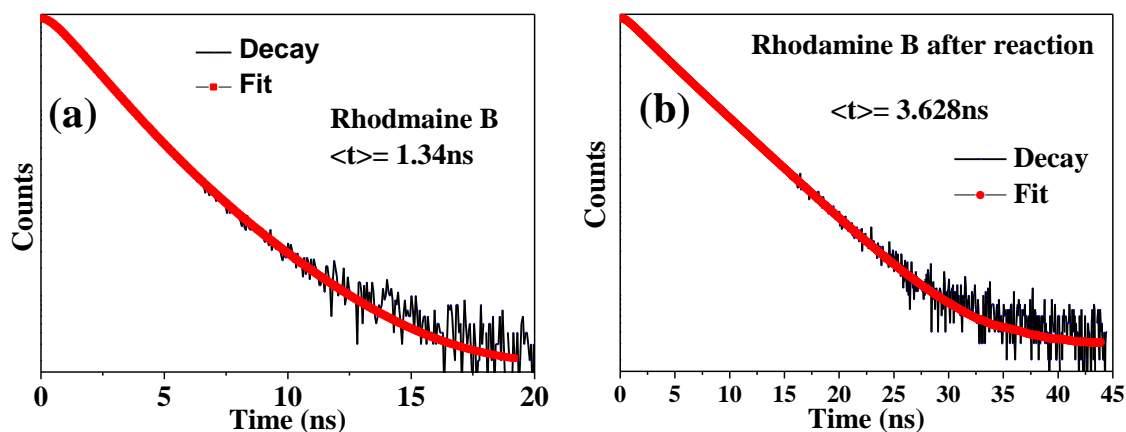


**Fig 4.17-** Fluorescence decay kinetics of (a) RhB and (b) solution after photoirradiation

## 4.2 Photocatalytic dye degradation by metal loaded $\text{Bi}_4\text{TaO}_8\text{Br}$

### 4.2.1 Powder X-ray Diffraction

The Powder X-ray diffraction patterns showed that the prepared orthorhombic  $\text{Bi}_4\text{TaO}_8\text{X}$  and metal loaded  $\text{Bi}_4\text{TaO}_8\text{Br}$  ( $\text{M}@\text{Bi}_4\text{TaO}_8\text{Br}$ ) are single phase as shown in the Figure 4.18. The XRD patterns of the metal deposited samples also illustrate that there are no diffraction peaks of the metal species can be observed. This is because the small crystallite size and low concentration of metal loading as also found in previous literature<sup>[88]</sup>.

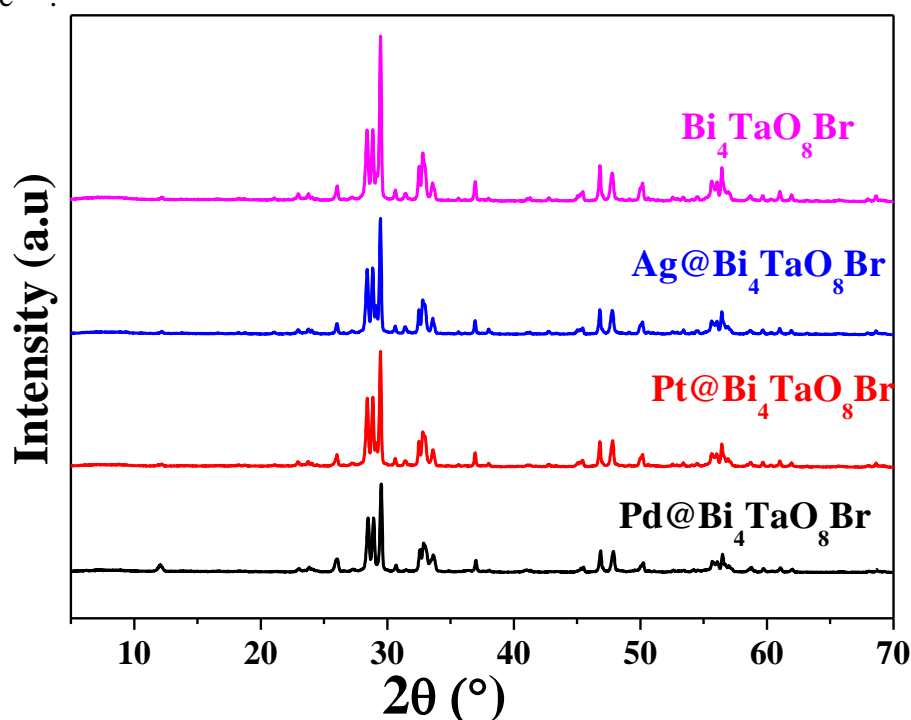


Fig 4.18- PXRD patterns of prepared  $\text{M}@\text{Bi}_4\text{TaO}_8\text{Br}$

### 4.2.2 Field Emission Scanning Electron Microscopy

The morphology and size of the samples were characterized by field emission scanning electron microscopy (FE- SEM). Figure 4.19 shows the metal loaded  $\text{Bi}_4\text{TaO}_8\text{Br}$  samples, with different sizes and morphology of the metal nanoparticles on the pure catalyst. For the  $\text{Ag}@\text{Bi}_4\text{TaO}_8\text{Br}$  sample, we observed rod like nanostructure with average size of 50 nm in length and 10 nm wide, which gives them high aspect ratio.  $\text{Pd}@\text{Bi}_4\text{TaO}_8\text{Br}$  samples have larger particles of Pd ~30 nm, and  $\text{Pt}@\text{Bi}_4\text{TaO}_8\text{Br}$  samples

were composed of nanoparticles of size  $\sim 5$  nm and was uniformly dispersed over the surface of  $\text{Bi}_4\text{TaO}_8\text{Br}$ .

The Energy Dispersive X-ray Spectroscopy was performed on a random assembly of the co-catalyst loaded samples which is composed of  $\sim 1.00$  wt% loading of the metal nanoparticles shown in Figure 4.20, and retained the stoichiometry of the prepared Bimuth Tantalum oxybromide.

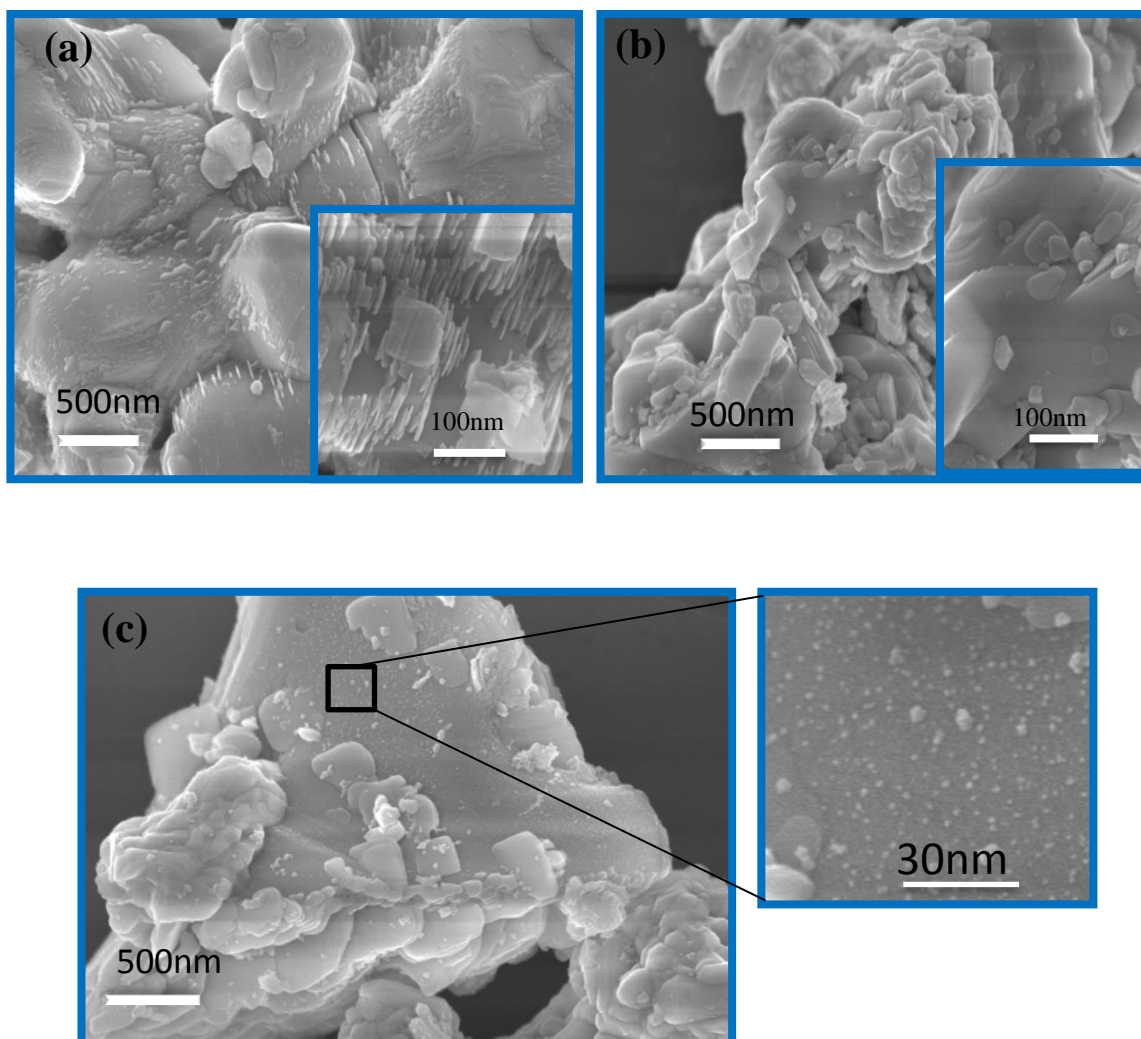


**Fig 4.19-** FE-SEM micrographs of (a)  $\text{Ag}@ \text{Bi}_4\text{TaO}_8\text{Br}$  (b)  $\text{Pd}@ \text{Bi}_4\text{TaO}_8\text{Br}$  and (c)  $\text{Pt}@ \text{Bi}_4\text{TaO}_8\text{Br}$ .

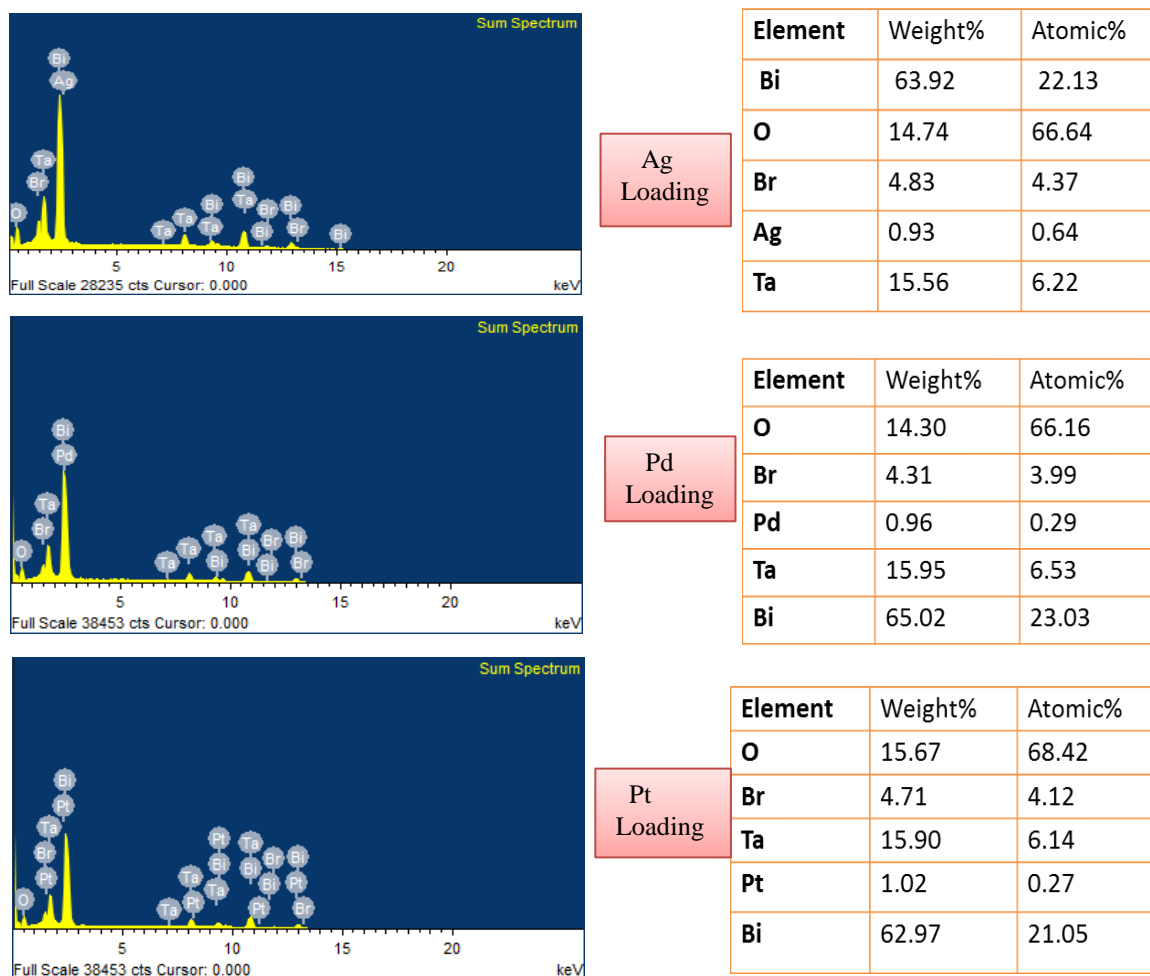


**Fig 4.20-** Elemental composition of (a) Ag@Bi<sub>4</sub>TaO<sub>8</sub>Br (b) Pd@Bi<sub>4</sub>TaO<sub>8</sub>Br and (c) Pt@Bi<sub>4</sub>TaO<sub>8</sub>Br obtained from EDS studies.

### 4.2.3 Diffuse Reflectance Spectroscopy

UV-Vis diffuse reflectance spectra (DRS) were carried out using a UV-Vis spectrometer by using BaSO<sub>4</sub> as a reference and were converted from reflection to absorbance by the Kubelka-Munk method. To calculate the optical band gap the following Tauc equation was used:

$$\alpha hv = A(hv - E_g)^{n/2}$$

where A = constant, hv = light energy, E<sub>g</sub> = optical band gap energy, α = measured absorption coefficient, for in-direct band gap materials. . In the equation, n reflects the



characteristics of the transition in a semiconductor, i.e.  $n = 1$  for direct transition and  $n = 4$  for indirect transition,  $M@Bi_4TaO_8Br$  is known as an indirect semiconductor.

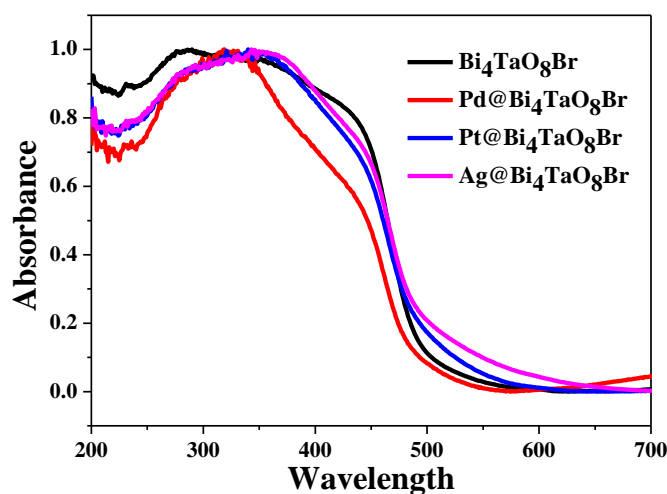


**Fig 4.20-** DRS plots of  $M@Bi_4TaO_8Br$  and bare  $Bi_4TaO_8Br$ .

In Figures 4.20 and 4.21, we show the optical absorption spectra and Tauc plots of  $Bi_4TaO_8Br$  and  $M@Bi_4TaO_8Br$ . It can be observed that according to the spectrum the absorption edge of the samples fall in the visible region of the spectrum, compared to the bare  $Bi_4TaO_8Br$ . Absorption originates from UV region and extends up to visible region which manifests that these materials have potential to show photocatalytic activity in the visible region. The observed band gaps are 2.45, 2.49, 2.50 and 2.52 eV of Pd, Pt, Ag and of  $Bi_4TaO_8Br$  respectively.

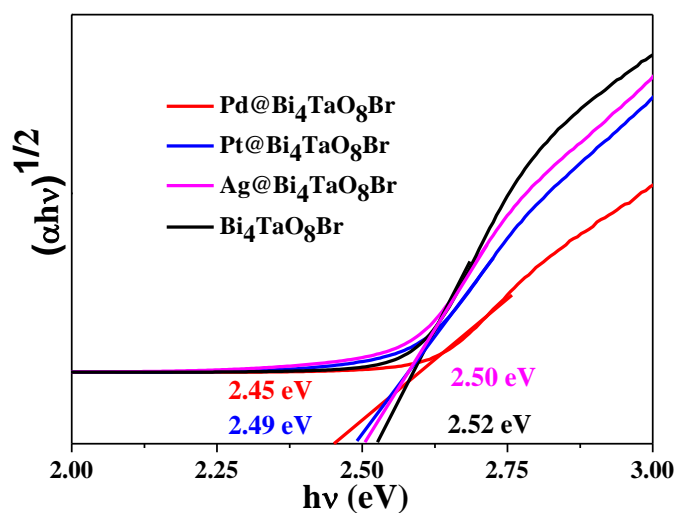


**Fig 4.21-** Tauc plot of  $M@Bi_4TaO_8Br$  and bare  $Bi_4TaO_8Br$ .

#### 4.2.4 Photoluminescence Properties

Photoluminescence emission spectra of photocatalysts helps to inspect the efficiency of charge carriers generated on illumination of light. It helps in understanding the trapping, migration and transfer of the electron and hole pairs in semiconductor photocatalyst. The room temperature photoluminescence emission spectra of  $M@Bi_4TaO_8Br$  are shown in Figure 4.22. The emitting maximum of the samples were observed at 562 nm when excited at 320 nm. The doping of metal results in the decrease in photoluminescence intensities as compared to the undoped one. It is observed from the plots that identical shapes and peak positions were observed over all the samples, but the emission peak intensities varied for the different metal loadings.

Palladium loaded  $Bi_4TaO_8Br$  caused the highest decrease of about ~11 times in the intensity of the photoluminescence peak at 562 nm compared to pure catalyst. The photoluminescence spectrum of a semiconductor can be ascribed to the radiative decay process, i.e. recombination of self-trapped excitations. Therefore, the presence of Pd, Pt and Ag metals on the photocatalyst decreases the radiative recombination process of the photogenerated electrons and holes. However, it should be noted that the above phenomenon is concentration dependent of the co-catalyst (metal), higher concentrations of these leads to new recombination centres and hence decreases the photocatalytic activity.

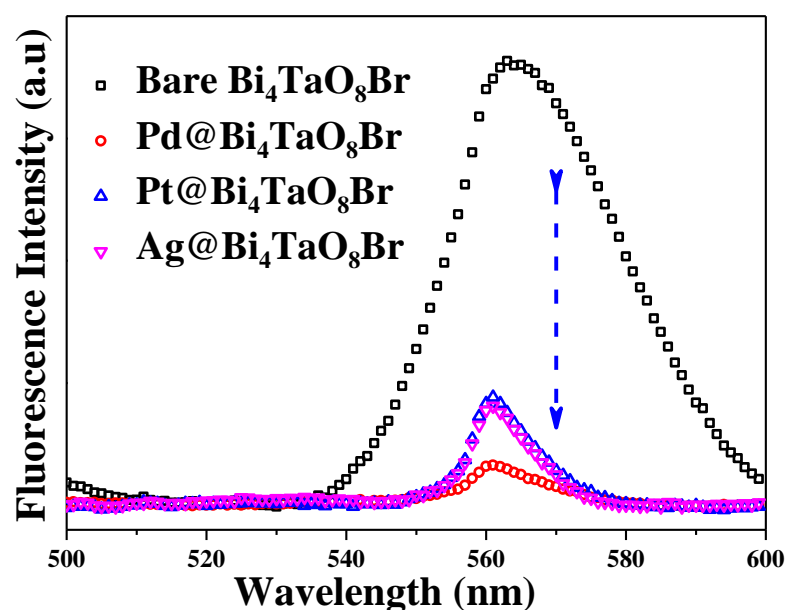


**Fig 4.22-** Photoluminescence spectra of  $M@Bi_4TaO_8Br$  and bare  $Bi_4TaO_8Br$ .

## 4.2.5 Photocatalytic Activity

The effects of depositing metal nanoparticles as co-catalyst on the photocatalytic activity of  $\text{Bi}_4\text{TaO}_8\text{Br}$  were evaluated by measuring the degradation of Rhodamine B in an aqueous solution of  $\text{pH}=2$  under visible light irradiation. Figure 4.23, shows temporal evolution of the spectral changes during the visible light photodegradation of RhB over the metal loaded photocatalysts. From this figure, it can be noted that the intensity of the absorption peak at 553 nm decreases drastically in few minutes of visible light irradiation, which indicates that this catalyst exhibits extremely high visible light photocatalytic activity. It is known that a dye photosensitization mechanism is closely related to the properties of the dye, such as the structural stability of the dye, the absorbability of the dye on catalyst surface, and the absorbance of the dye. So to confirm that is not photosensitization, we carried out control experiments in absence of light and in absence of catalyst (only visible light irradiation of dye solution) which confirms that this dye mineralization is occurring only via photocatalysis.

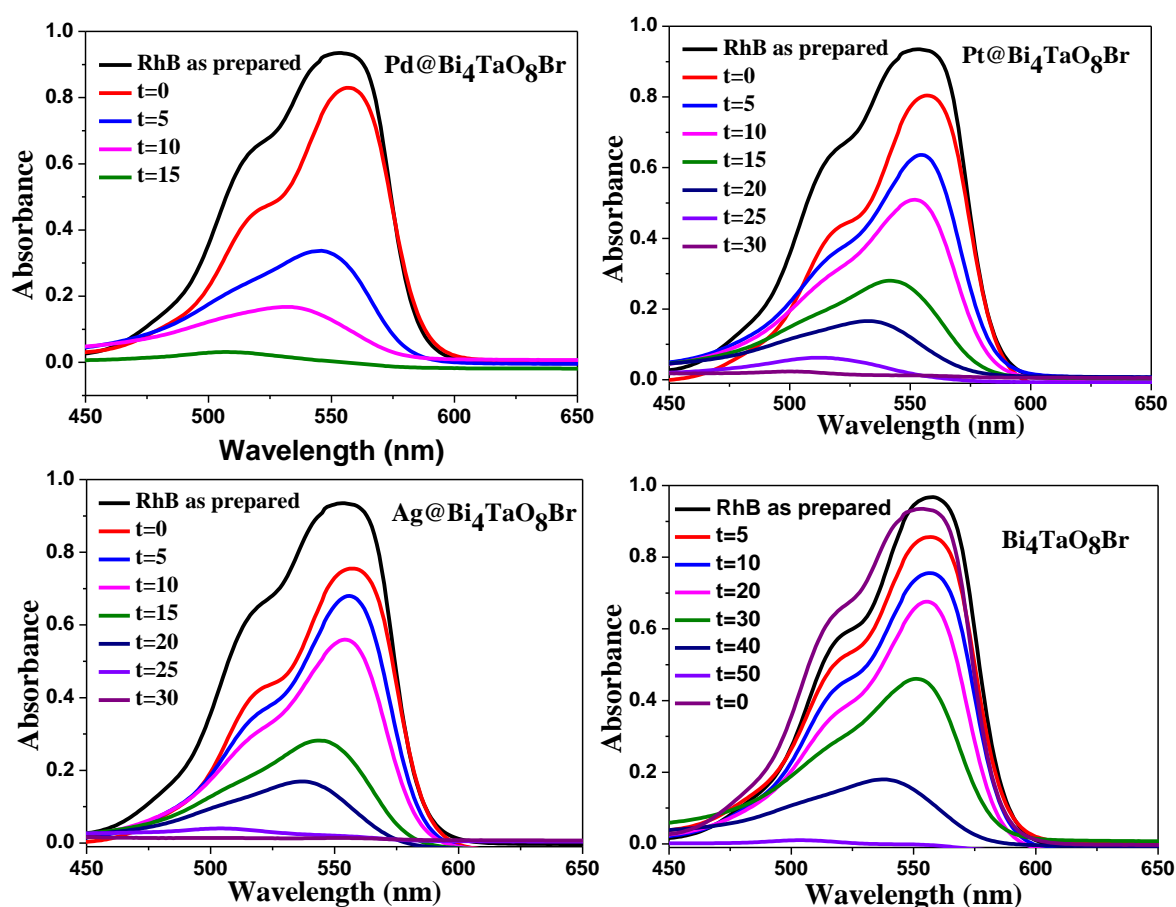


**Fig 4.23-** Temporal UV-Visible spectra of RhB degradation by Metal loaded and bare  $\text{Bi}_4\text{TaO}_8\text{Br}$ .

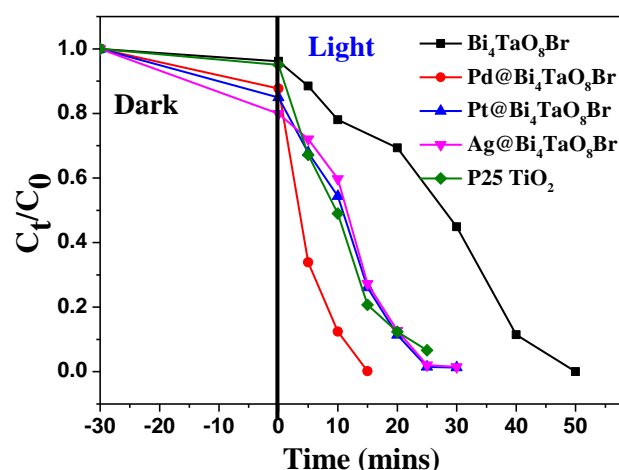


**Fig 4.24-** Photocatalytic RhB degradation by Metal loaded and bare  $\text{Bi}_4\text{TaO}_8\text{Br}$ .

To quantitatively understand the photocatalytic reaction kinetics of RhB degradation under visible-light irradiation, the following pseudo first-order model<sup>[119]</sup> was used to analyse our photocatalytic degradation data:

$$\ln\left(\frac{C_0}{C_t}\right) = k_1 t$$

(where  $k_1$  = pseudo-first-order rate constant; and  $C_0$ : the initial concentration of RhB,  $C_t$ : the RhB dye concentration at any time ( $t$ )). The results with visible light irradiation are displayed in Figure 4.25. A good correlation to the pseudo first-order reaction kinetics was found for RhB in the presence of  $\text{M@Bi}_4\text{TaO}_8\text{Br}$ . The removal rate of RhB by  $\text{Pd@Bi}_4\text{TaO}_8\text{Br}$  is much higher than rates by  $\text{Pt@Bi}_4\text{TaO}_8\text{Br}$ ,  $\text{Ag@Bi}_4\text{TaO}_8\text{Br}$  and bare  $\text{Bi}_4\text{TaO}_8\text{Br}$ .

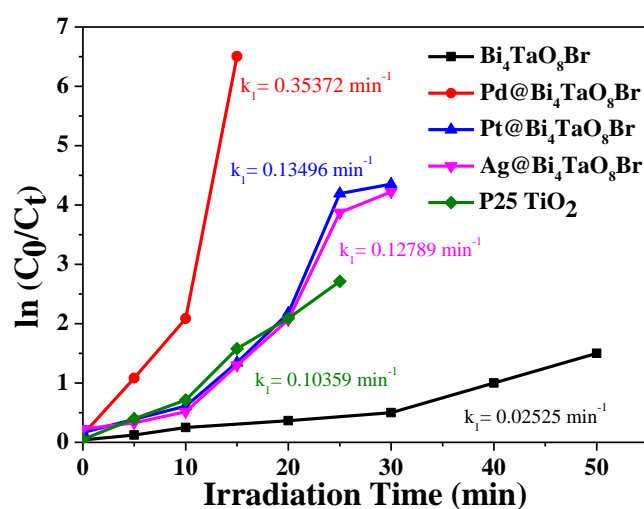


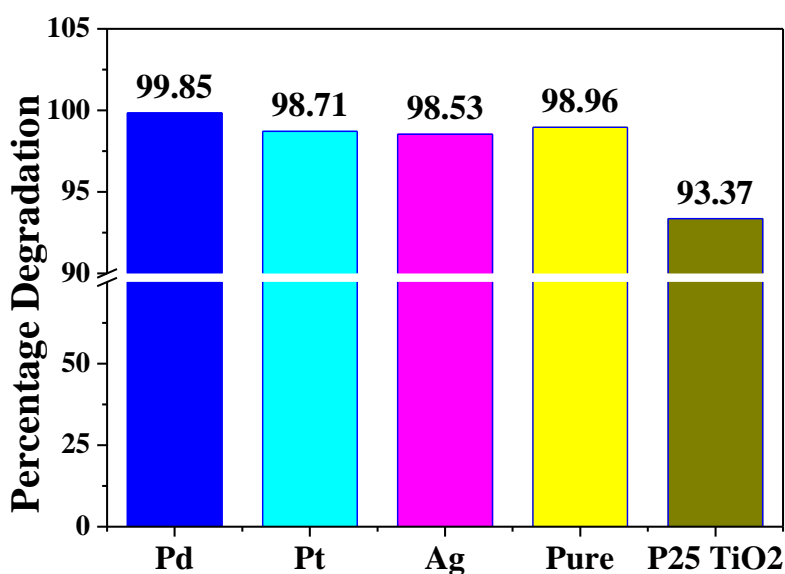
**Fig 4.25-** Plot of  $\ln(C_0/C_t)$  as a function of irradiation time of  $\text{M@Bi}_4\text{TaO}_8\text{Br}$ , bare  $\text{Bi}_4\text{TaO}_8\text{Br}$  and  $\text{P25 TiO}_2$ .

Further, we compared our loaded catalysts with commercially available P25 TiO<sub>2</sub> shown in Figure 4.25. We observed that the Pd@BiaTaO<sub>8</sub>Br catalyst outperformed the commercial state-of-the-art P25 TiO<sub>2</sub> having rate constant 0.10359 min<sup>-1</sup>, while 0.35372 min<sup>-1</sup> for Pd@BiaTaO<sub>8</sub>Br. The enhanced activity is mainly due to its strong adsorption of light in the visible light region and low lying Fermi energy levels of Pd, assisting the migration of photogenerated electrons from the CB to the surface of Pd. Thus, the electron–hole separation is enhanced which improved the photocatalytic activity of the compound. The observed rates are 0.35372 min<sup>-1</sup>, 0.13496 min<sup>-1</sup> and 0.12789 min<sup>-1</sup> for Pd, Pt and Ag@Bi<sub>4</sub>TaO<sub>8</sub>Br respectively. All metal deposited samples show much higher photocatalytic activity than that of the pure sample.

Here, we define the dye degradation efficiency by:

$$D = \left( \frac{C_0 - C_t}{C_0} \right) \times 100$$

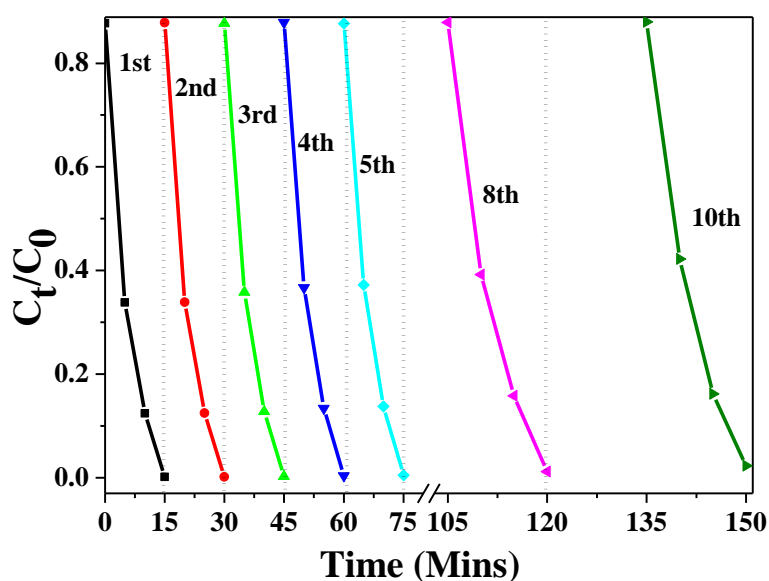
(where D: degradation efficiency, C<sub>0</sub>: the initial concentration of RhB, C<sub>t</sub>: the RhB dye concentration at any time (t)). The degradation efficiency of the catalysts are 99.85%, 98.71%, 98.53%, 98.96%, 93.37% for Pd, Pt, Ag, Pure and P25 TiO<sub>2</sub> respectively, shown in Figure 4.26. So the deposition of 1.0 wt% co-catalyst brought about significant enhancement in the rate of the degradation. Pd@Bi<sub>4</sub>TaO<sub>8</sub>Br demonstrated 3 times faster rate constant than the commercial state-of-the-art P25 TiO<sub>2</sub>.



**Fig 4.26-** Plot of percentage degradation of RhB by M@Bi<sub>4</sub>TaO<sub>8</sub>Br, bare Bi<sub>4</sub>TaO<sub>8</sub>Br and P25 TiO<sub>2</sub>.

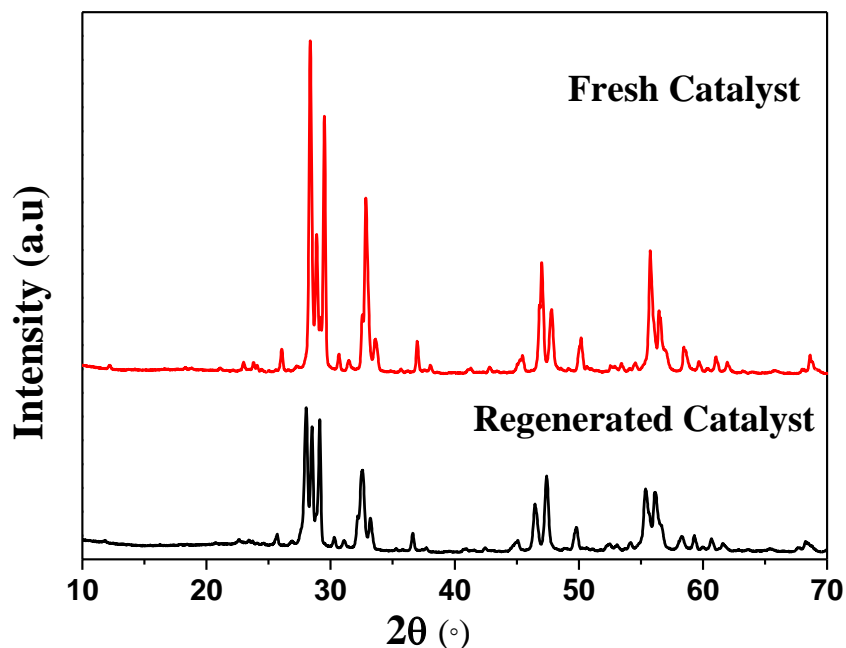
## 4.2.6 Stability Test and Product analysis

The stability of photocatalysts is an important yardstick to be evaluated for their commercialization. The recyclability of the photocatalytic RhB degradation was carried out as shown in Figure 4.27. After 10 cycles the Pd@BTaO8Br sample demonstrated excellent reusability of the catalyst. A negligible loss of 2.15% in activity was observed in the 10th cycle, which can be attributed to the loss of some amount of catalyst during reusability. The PXRD pattern of Pd@Bi<sub>4</sub>TaO<sub>8</sub>Br after the recycling experiments is provided in the Figure 4.28.



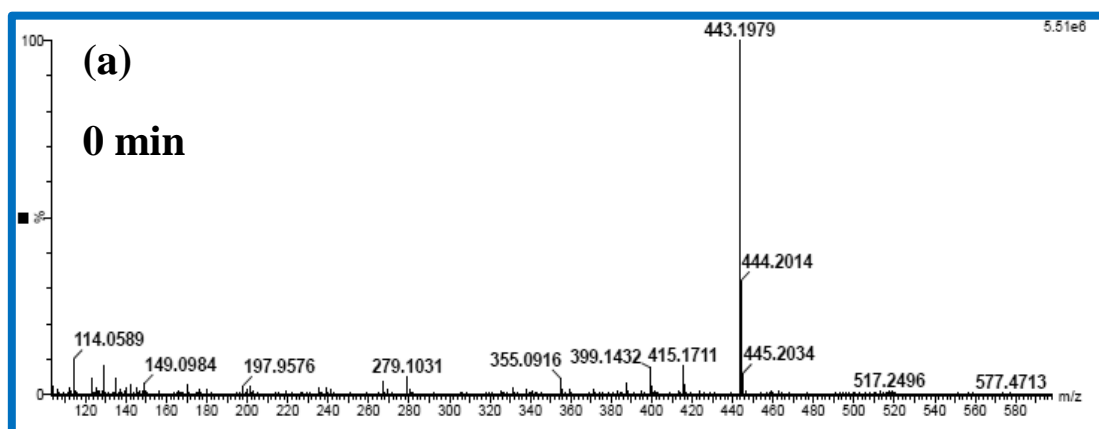
**Fig 4.27-** Plot of cyclic stability test for degradation of RhB by Pd@Bi<sub>4</sub>TaO<sub>8</sub>Br.

The unusual band structure of Bi<sub>4</sub>TaO<sub>8</sub>Br seems to play an important role on the stability during photocatalytic activity. In previous literature mixed anion materials such as oxynitrides<sup>[120]</sup>, oxysulfides<sup>[121]</sup>, or oxyhalides<sup>[95]</sup> has majority contribution of p-orbitals of the non-oxide anions on VBM having lesser electronegativity compared to Oxygen. As a consequence the photogenerated holes around VBM are prone to self-oxidize these ions during the photocatalysis e.g.,  $2N^{3-} + 6h^+ \rightarrow N_2$ ,  $2X^- + 2h^+ \rightarrow X_2$  resulting in photocorrosion to give an inactive surface. On the contrary, the VBM of Bi<sub>4</sub>TaO<sub>8</sub>Br is mainly composed of the dispersive O-2p band. As a result, we observe enhanced photocatalytic dye degradation efficacy.



**Fig 4.28-** PXRD pattern of Fresh and Regenerated Pd@Bi<sub>4</sub>TaO<sub>8</sub>Br.

To analyse the species produced in the photodegradation of RhB, the temporal High Resolution Mass Spectrometry profiles of the dye, intermediates, and final products were monitored as shown in Figure 4.29. RhB has its characteristic molecular ion peak at 443 m/z, which vanishes under visible light irradiation, and new peaks arise at 325, 355, 179 m/z. The change in the mass spectrometry was examined at specific time intervals of the photocatalysis revealed the removal of RhB. Based on the HRMS data, it can be inferred that RhB undergoes degradation to small oxidized molecules such as 4-(methoxycarbonyl) benzoic acid (179 m/z), 2-(methoxycarbonyl) benzoic acid (179 m/z), benzoic acid (123 m/z), 2,6-dimethyl phenol (123 m/z) etc.



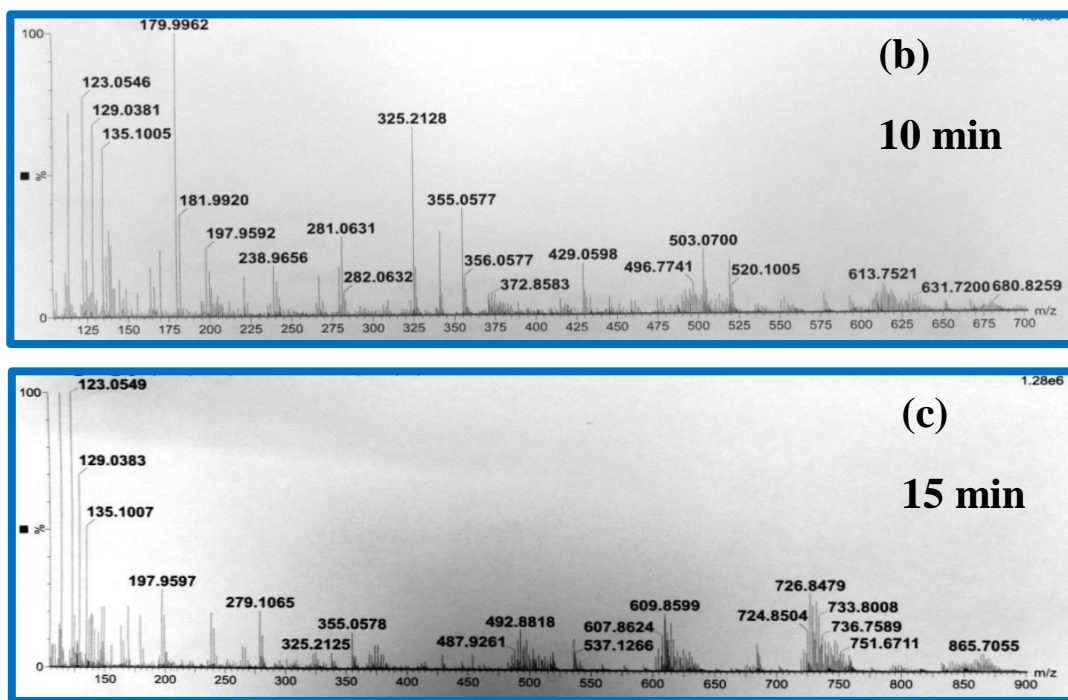


**Fig 4.29-** HRMS spectra collected at different intervals (a) 0 min; (b) after 10 min; (c) after 15 min photoirradiation using Pd@ Bi<sub>4</sub>TaO<sub>8</sub>Br.

#### 4.2.7 Photocatalytic Degradation Mechanism

It is well known that superoxide radical anions ( $O_2^{\bullet-}$ ), holes ( $h^+$ ) and hydroxyl radicals ( $OH^{\bullet}$ ) are among the main reactive species that play major role in the photocatalytic dye degradation process. So, to understand the role of various reactive species in visible-driven RhB degradation various scavenger tests were performed over Bi<sub>4</sub>TaO<sub>8</sub>Br. Figure 4.30 represents trapping experiments using various scavengers under visible light. Ammonium oxalate, tertiary butanol and benzoquinone were used as holes ( $h^+$ ), hydroxyl radicals ( $OH^{\bullet}$ ) and superoxide radical anions ( $O_2^{\bullet-}$ ). It can be observed from the Figure 4.30 that addition of hydroxyl radicals ( $OH^{\bullet}$ ) scavenger did not have much effect on the degradation of Rhodamine dye. However, dye degradation was inhibited upon addition of holes scavenger and superoxide radical anions scavenger. These observations of scavenger experiments indicated holes ( $h^+$ ) and superoxide radical anions ( $O_2^{\bullet-}$ ) as the dominant species playing active role in the RhB degradation under



visible light in presence of  $\text{Bi}_4\text{TaO}_8\text{Br}$ . Based on these trapping experiments we have proposed a mechanism of the degradation process as shown below:

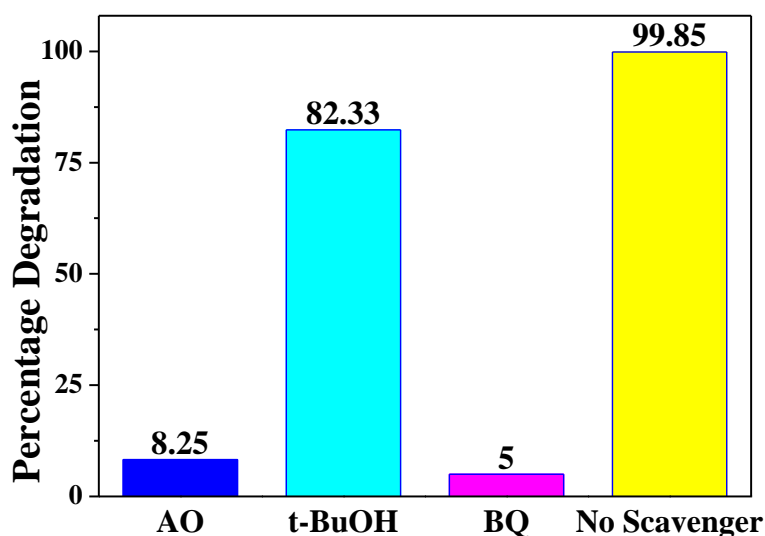
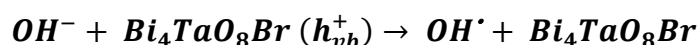
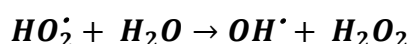
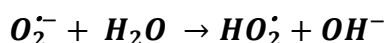
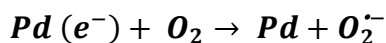
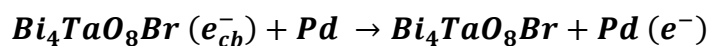


**Fig 4.30-** Percentage degradation using different scavenger using  $\text{Pd@Bi}_4\text{TaO}_8\text{Br}$ .

The presence of Pd, Pt and Ag deposited on  $\text{Bi}_4\text{TaO}_8\text{Br}$  is believed to retard the fast charge-pair recombination by serving as an electron sink (Schottky barrier electron trapping) and to facilitate the interfacial electron transfer to dioxygen or other electron acceptors, which has been supported by electrochemical and time-resolved spectroscopic investigations on extensively studied  $\text{TiO}_2$ . It is known that the photocatalytic activities of photocatalyst are primarily regulated by the ratio of surface electron transfer rate to the exciton recombination rate. So if the transfer of electrons in the surface of the catalyst is

fast, it enhances the overall catalytic reaction. And, it is been known that the dispersed metal nanoparticles loaded onto the photocatalyst act as deep electron trap states which facilitate the electron and hole separation. Hence, introduction of a small amount of Pd/Pt/Ag leads to significant improvement in the photocatalytic activity. Further, if concentration or loading amount of co-catalyst is high it forms overlapping agglomerates and leads to the loss of surface area and formation of new recombination centres, which give a negative effect on the activity of catalyst. So, in accordance to the discussion a possible mechanism of the enhancement of photocatalysis by Pd@Bi<sub>4</sub>TaO<sub>8</sub>Br is elucidated in Figure 4.30.

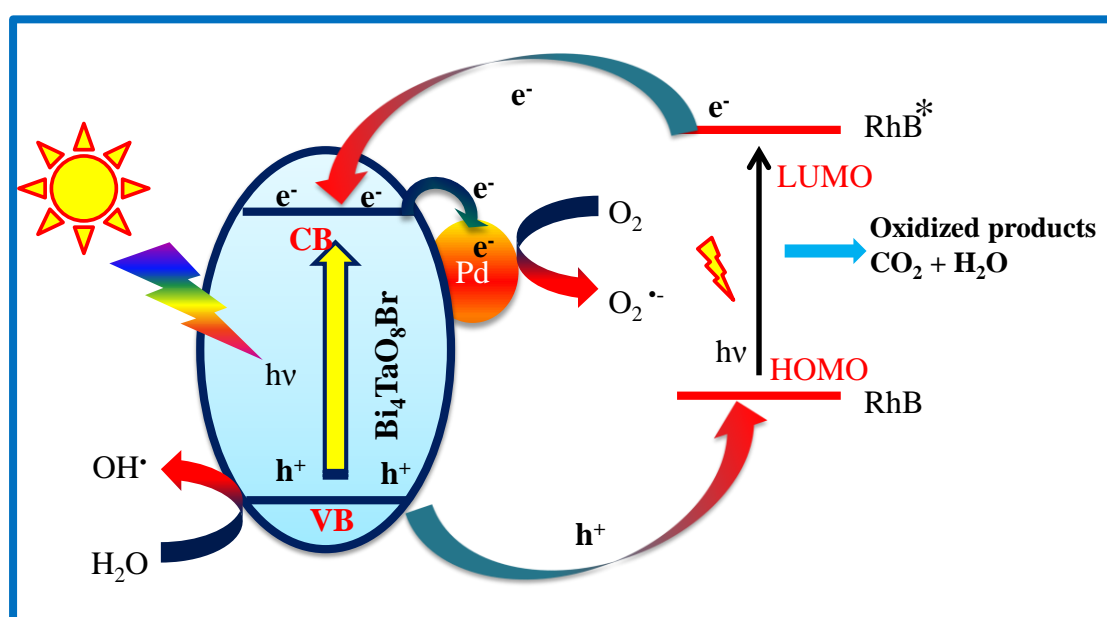


**Fig 4.30-** Schematic representation of the photocatalytic RhB degradation mechanism.

The electrons in the valence band of Bi<sub>4</sub>TaO<sub>8</sub>Br are excited in presence of light and gets transfer to conduction band. Introducing co-catalyst such as Pd, Pt and Ag facilitates the trapping of electrons in the deep states (of metals) stimulating the electron–hole separation and subsequently transfers the trapped electron to the adsorbed O<sub>2</sub> which act as an electron acceptor on the surface of the Bi<sub>4</sub>TaO<sub>8</sub>Br. The generated O<sub>2</sub><sup>•-</sup> oxidises the RhB into smaller fragments. On the other hand, the active species such as OH<sup>•</sup> and h<sup>+</sup> formed also degrade the organic compound. Thus we observed the overall rate in the order Pd@Bi<sub>4</sub>TaO<sub>8</sub>Br > Pt@Bi<sub>4</sub>TaO<sub>8</sub>Br > Ag@Bi<sub>4</sub>TaO<sub>8</sub>Br > Bi<sub>4</sub>TaO<sub>8</sub>Br.

## 5. CONCLUSION

In this study, we have synthesised Sillen-Aurivillius layered perovskite  $\text{Bi}_4\text{TaO}_8\text{Br}$  and its metal loaded analogue ( $\text{M}@\text{Bi}_4\text{TaO}_8\text{Br}$ ) using Solid-state and photodeposition techniques. We have used the solvothermal route to synthesise the Bismuth oxyhalide ( $\text{BiOBr}$ ) precursor. The prepared materials were further characterised by PXRD, FESEM, EDS, DRS and was found to be micrometre size polycrystalline solid with band gap in the visible region. The photocatalytic activity of the prepared photocatalysts was checked using a model reaction that involves degradation of toxic pollutants and photochemical organic transformation to prepare fine chemicals.

RhB is considered as a potential hazardous waste and toxic pollutant which are released from industrial manufacturers such as textile industry. The conversion of RhB to Rh110 is important because Rh110 is extensively used in biological research due to its excellent photophysical property. The unique application of Rh110 is its use as a latent fluorophore, which is exceptionally advantageous over other xanthene based dyes. The efficiency of the photocatalyst was measured by recording UV-Vis plots along with the calculation of rate constant and percentage yield at varying pH.

We have obtained a yield of 40% at a  $\text{pH}=7$  for the conversion of RhB to Rh110 using  $\text{Bi}_4\text{TaO}_8\text{Br}$ . Moreover,  $\text{Pd}@\text{Bi}_4\text{TaO}_8\text{Br}$  exhibit excellent photocatalytic activity for the degradation of RhB dye with a rate constant of  $0.35372 \text{ min}^{-1}$  surpassing commercial state-of-the-art P25  $\text{TiO}_2$  ( $0.10359 \text{ min}^{-1}$ ). Such high activity of Pd loaded catalyst is believed to be due to the presence of various active sites on its surface, owing to efficient electron transfer from CB of catalyst to the Fermi level of Pd which helps in effective separation of electron-hole pairs. We have also performed the stability tests of our catalyst and, we observed that the catalyst could be reused up to 10 cycles of photocatalysis. Even after the 10 catalytic cycles, we can regain the photocatalytic activity by firing the catalyst at  $750^\circ\text{C}$  in open air for 5 mins.

As commercial catalysts have drawbacks like photocorrosion, poor visible light absorption, this prepared photocatalyst can be a potential alternative them due to its excellent photocatalytic activity, visible light absorption and stability.

## 6. SCOPE FOR FUTURE WORK

This thesis attempted to investigate the photocatalytic properties of layered *Sillen-Aurivillius* perovskite phases. The thesis investigates the structural influence on photocatalysis, thereby finding insights to understand the fundamental aspects of impact of the crystallite size, crystal structure and band gap to tune its photocatalytic activity.

The work on the transformation of RhB to Rh110 can pave a way to the synthesis of newer, important fine chemicals using solar energy. This methodology can be extensively used for the synthesis of expensive chemicals using a readily available cheaper variant. Secondly, photocatalytic degradation of toxic pollutants was carried out by mobilising the solid catalyst in the aqueous solution which may limit its practical application as the catalyst can be washed away with the polluted effluent. So to prevent such percolating of the catalyst material, the photocatalyst may be immobilised over a substrate such as a ceramic sheet or glass plate for practical applications.

Further, these photocatalysts can be used efficiently for solar energy harvesting reactions such as water splitting, CO<sub>2</sub> reduction, N<sub>2</sub> fixation etc.

## 7. BIBLIOGRAPHY

- [1] P. A. Deshpande, G. Madras, *Chem. Eng. J.* **2010**, *158*, 571–577.
- [2] R. Dillert, D. Bahnemann, H. Hidaka, *Chemosphere* **2007**, *67*, 785–792.
- [3] H. Fu, C. Pan, W. Yao, Y. Zhu, *J. Phys. Chem. B* **2005**, *109*, 22432–22439.
- [4] Joseph B, *Environmental Studies*, Tata McGraw-Hill Education Pvt. Ltd., 2008, **2009**.
- [5] G. of India, *Schedule of the Environment Protection Rules, 1989*, **1989**.
- [6] W. Stumm, H. Huper, R. L. Champlin, *Environ. Sci. Technol.* **1967**, *1*, 221–227.
- [7] A. Sommerauer, D. L. Sussman, W. Stumm, *Kolloid-Zeitschrift und Zeitschrift für Polym.* **1968**, *225*, 147–154.
- [8] F. I. Hai, K. Yamamoto, K. Fukushi, *Crit. Rev. Environ. Sci. Technol.* **2007**, *37*, 315–377.
- [9] P. Le-Clech, E.-K. Lee, V. Chen, *Water Res.* **2006**, *40*, 323–330.
- [10] T. Melin, B. Jefferson, D. Bixio, C. Thoeye, W. De Wilde, J. De Koning, J. van der Graaf, T. Wintgens, *Desalination* **2006**, *187*, 271–282.
- [11] P. A. Carneiro, R. F. P. Nogueira, M. V. B. Zanoni, *Dye. Pigment.* **2007**, *74*, 127–132.
- [12] S. E. Jørgensen, *Industrial Waste Water Management*, Elsevier, **1979**.
- [13] J. F. Judkins, *J. Water Pollut. Control Fed.* **1982**, *54*, 702–704.
- [14] S. Zhang, X. Liu, M. Wang, B. Wu, B. Pan, H. Yang, H.-Q. Yu, *Environ. Sci. Technol. Lett.* **2014**, *1*, 167–171.
- [15] A. V. Rupa, D. Divakar, T. Sivakumar, *Catal. Letters* **2009**, *132*, 259–267.
- [16] G. Moon, D. Kim, H. Kim, A. D. Bokare, W. Choi, *Environ. Sci. Technol. Lett.* **2014**, *1*, 185–190.
- [17] M. Styliidi, D. I. Kondarides, X. E. Verykios, *Appl. Catal. B Environ.* **2003**, *40*, 271–286.
- [18] A. Wilkinson, A. ; McNaught, *IUPAC Compendium of Chemical Terminology*, Blackwell Scientific Publications, Oxford, UK, **1997**.
- [19] J. Verhoeven, *Pure Appl. Chem.* **1996**, *68*, 2223.
- [20] L. Yin, Z. Shen, J. Niu, J. Chen, Y. Duan, *Environ. Sci. Technol.* **2010**, *44*, 9117–9122.
- [21] C. C. Wong, W. Chu, *Chemosphere* **2003**, *50*, 981–987.
- [22] R.-J. Wu, C.-C. Chen, C.-S. Lu, P.-Y. Hsu, M.-H. Chen, *Desalination* **2010**, *250*,

- 869–875.
- [23] T. Wu, G. Liu, J. Zhao, H. Hidaka, N. Serpone, *J. Phys. Chem. B* **1998**, *102*, 5845–5851.
- [24] Q. Xiao, J. Zhang, C. Xiao, Z. Si, X. Tan, *Sol. Energy* **2008**, *82*, 706–713.
- [25] Y. Xie, C. Yuan, *Appl. Catal. B Environ.* **2003**, *46*, 251–259.
- [26] A. Fujishima, K. Honda, *Nature* **1972**, *238*, 37.
- [27] S. N. Frank, A. J. Bard, *J. Am. Chem. Soc.* **1977**, *99*, 303–304.
- [28] K. Kabra, R. Chaudhary, R. L. Sawhney, *Ind. Eng. Chem. Res.* **2004**, *43*, 7683–7696.
- [29] M. R. Hoffmann, S. T. Martin, W. Choi, D. W. Bahnemann, *Chem. Rev.* **1995**, *95*, 69–96.
- [30] Y. Kuwahara, T. Kamegawa, K. M. and H. Yamashita, *Curr. Org. Chem.* **2010**, *14*, 616–629.
- [31] T. Sivakumar, K. Shanthi, T. Newton Samuel, *Bioprocess Eng.* **2000**, *23*, 579–583.
- [32] W. Y. Teoh, J. A. Scott, R. Amal, *J. Phys. Chem. Lett.* **2012**, *3*, 629–639.
- [33] K. Boer, *Survey of Semiconductor Physics*, Van Nostrand Reinhold, Springer Netherlands, **1990**.
- [34] X. Li, J. Yu, J. Low, Y. Fang, J. Xiao, X. Chen, *J. Mater. Chem. A* **2015**, *3*, 2485–2534.
- [35] R. Hill, F. A. Y. Bendall, *Nature* **1960**, *187*, 417.
- [36] S. A. Barber, *Soil Nutrient Bioavailability: A Mechanistic Approach*, John-Wiley & Sons, New York, **1995**.
- [37] H. Kato, M. Hori, R. Konta, Y. Shimodaira, A. Kudo, *Chem. Lett.* **2004**, *33*, 1348–1349.
- [38] L. Ye, J. Liu, C. Gong, L. Tian, T. Peng, L. Zan, *ACS Catal.* **2012**, *2*, 1677–1683.
- [39] J. Zhu, M. Zäch, *Curr. Opin. Colloid Interface Sci.* **2009**, *14*, 260–269.
- [40] H. Tada, T. Mitsui, T. Kiyonaga, T. Akita, K. Tanaka, *Nat. Mater.* **2006**, *5*, 782.
- [41] Y. Sasaki, A. Iwase, H. Kato, A. Kudo, *J. Catal.* **2008**, *259*, 133–137.
- [42] A. Iwase, Y. H. Ng, Y. Ishiguro, A. Kudo, R. Amal, *J. Am. Chem. Soc.* **2011**, *133*, 11054–11057.
- [43] Z. Peng, Y. Jianguo, J. Mietek, *Adv. Mater.* **2014**, *26*, 4920–4935.
- [44] K. Maeda, *ACS Catal.* **2013**, *3*, 1486–1503.
- [45] H. Zhu, B. Yang, J. Xu, Z. Fu, M. Wen, T. Guo, S. Fu, J. Zuo, S. Zhang, *Appl. Catal. B Environ.* **2009**, *90*, 463–469.

- [46] C.-C. Hu, H. Teng, *J. Catal.* **2010**, 272, 1–8.
- [47] K. Sekizawa, K. Maeda, K. Domen, K. Koike, O. Ishitani, *J. Am. Chem. Soc.* **2013**, 135, 4596–4599.
- [48] M. Miyauchi, Y. Nukui, D. Atarashi, E. Sakai, *ACS Appl. Mater. Interfaces* **2013**, 5, 9770–9776.
- [49] A. Kudo, *MRS Bull.* **2011**, 36, 32–38.
- [50] F. Sayilkan, M. Asiltürk, P. Tatar, N. Kiraz, Ş. Şener, E. Arpaç, H. Sayilkan, *Mater. Res. Bull.* **2008**, 43, 127–134.
- [51] X. Yao, X. Wang, L. Su, H. Yan, M. Yao, *J. Mol. Catal. A Chem.* **2011**, 351, 11–16.
- [52] L. G. Devi, B. N. Murthy, S. G. Kumar, *J. Mol. Catal. A Chem.* **2009**, 308, 174–181.
- [53] A. Zaleska-Medynska, *Recent Patents Eng.* **2008**, 2, 157–164.
- [54] B.-S. Huang, E.-C. Su, M.-Y. Wey, *Chem. Eng. J.* **2013**, 223, 854–859.
- [55] M. Behnajady, N. Modirshahla, M. Shokri, B. Rad, *Glob. Nest J.* **2008**, 10, 1–7.
- [56] M. A. Barakat, H. Schaeffer, G. Hayes, S. Ismat-Shah, *Appl. Catal. B Environ.* **2005**, 57, 23–30.
- [57] J. Choi, H. Park, M. R. Hoffmann, *J. Phys. Chem. C* **2010**, 114, 783–792.
- [58] V. Mirkhani, S. Tangestaninejad, M. Moghadam, M. H. Habibi, A. Rostami-Vartooni, *J. Iran. Chem. Soc.* **2009**, 6, 578–587.
- [59] K. H. Drexhage, *Fluorescence Efficiency of Laser Dyes*, **1976**.
- [60] K. H. Drexhage, *Laser Focus* **1973**, 9, 35–39.
- [61] G. A. Crosby, J. N. Demas, *J. Phys. Chem.* **1971**, 75, 991–1024.
- [62] T. J. V Prazeres, A. Fedorov, S. P. Barbosa, J. M. G. Martinho, M. N. Berberan-Santos, *J. Phys. Chem. A* **2008**, 112, 5034–5039.
- [63] S. Lorey, J. Faust, C. Mrestani-Klaus, T. Kähne, S. Ansorge, K. Neubert, F. Bühling, *J. Biol. Chem.* **2002**, 277, 33170–33177.
- [64] A. P. Guzikowski, J. J. Naleway, C. T. Shipp, R. C. Schutte, *Tetrahedron Lett.* **2000**, 41, 4733–4735.
- [65] S. X. Cai, H.-Z. Zhang, J. Guastella, J. Drewe, W. Yang, E. Weber, *Bioorg. Med. Chem. Lett.* **2001**, 11, 39–42.
- [66] S. S. Chandran, K. A. Dickson, R. T. Raines, *J. Am. Chem. Soc.* **2005**, 127, 1652–1653.
- [67] M. M. Yatzeck, L. D. Lavis, T.-Y. Chao, S. S. Chandran, R. T. Raines, *Bioorg.*

- Med. Chem. Lett.* **2008**, *18*, 5864–5866.
- [68] H.-Z. Zhang, S. Kasibhatla, J. Guastella, B. Tseng, J. Drewe, S. X. Cai, *Bioconjug. Chem.* **2003**, *14*, 458–463.
- [69] L. D. Lavis, T.-Y. Chao, R. T. Raines, *ACS Chem. Biol.* **2006**, *1*, 252–260.
- [70] S. L. Mangold, R. T. Carpenter, L. L. Kiessling, *Org. Lett.* **2008**, *10*, 2997–3000.
- [71] J. Fenneteau, D. Chauvin, A. D. Griffiths, C. Nizak, J. Cossy, *Chem. Commun.* **2017**, *53*, 5437–5440.
- [72] W. L. M., G. J. B., T. A. N., B. T. A., B. Eric, L. L. D., *Angew. Chemie Int. Ed.* **2011**, *50*, 11206–11209.
- [73] Y. Yang, J. O. Escobedo, A. Wong, C. M. Schowalter, M. C. Touchy, L. Jiao, W. E. Crowe, F. R. Fronczek, R. M. Strongin, *J. Org. Chem.* **2005**, *70*, 6907–6912.
- [74] H. Braun, J. v.;K., M. E., *Berichte der Dtsch. Chem. Gesellschaft* **1918**, *51*, 273–282.
- [75] A. Shibata, K. Furukawa, H. Abe, S. Tsuneda, Y. Ito, *Bioorg. Med. Chem. Lett.* **2008**, *18*, 2246–2249.
- [76] K. K. Kim, J. O. Escobedo, N. N. St. Luce, O. Rusin, D. Wong, R. M. Strongin, *Org. Lett.* **2003**, *5*, 5007–5010.
- [77] T. L. Halo, J. Appelbaum, E. M. Hobert, D. M. Balkin, A. Schepartz, *J. Am. Chem. Soc.* **2009**, *131*, 438–439.
- [78] B. Tang, Y. Xing, P. Li, N. Zhang, F. Yu, G. Yang, *J. Am. Chem. Soc.* **2007**, *129*, 11666–11667.
- [79] S. Craig, M. Eric, *Angew. Chemie Int. Ed.* **2006**, *45*, 5645–5648.
- [80] M. M. Pires, J. Chmielewski, *Org. Lett.* **2008**, *10*, 837–840.
- [81] M. Beija, C. A. M. Afonso, J. M. G. Martinho, *Chem. Soc. Rev.* **2009**, *38*, 2410–2433.
- [82] T. Watanabe, T. Takizawa, K. Honda, *J. Phys. Chem.* **1977**, *81*, 1845–1851.
- [83] C. Yu, J. C. Yu, M. Chan, *J. Solid State Chem.* **2009**, *182*, 1061–1069.
- [84] C. Yu, J. C. Yu, *Catal. Letters* **2009**, *129*, 462.
- [85] M. Li, S. Zhou, Y. Zhang, G. Chen, Z. Hong, *Appl. Surf. Sci.* **2008**, *254*, 3762–3766.
- [86] C. Yu, J. C. Yu, *Mater. Sci. Eng. B* **2009**, *164*, 16–22.
- [87] M. N. Chong, B. Jin, C. W. K. Chow, C. Saint, *Water Res.* **2010**, *44*, 2997–3027.
- [88] C. Yu, J. C. Yu, C. Fan, H. Wen, S. Hu, *Mater. Sci. Eng. B* **2010**, *166*, 213–219.
- [89] F. E. Osterloh, *Chem. Mater.* **2008**, *20*, 35–54.



- [90] R. Abe, *J. Photochem. Photobiol. C Photochem. Rev.* **2010**, *11*, 179–209.
- [91] A. Kudo, Y. Miseki, *Chem. Soc. Rev.* **2009**, *38*, 253–278.
- [92] K. Maeda, K. Teramura, D. Lu, T. Takata, N. Saito, Y. Inoue, K. Domen, *Nature* **2006**, *440*, 295.
- [93] Y. Lee, H. Terashima, Y. Shimodaira, K. Teramura, M. Hara, H. Kobayashi, K. Domen, M. Yashima, *J. Phys. Chem. C* **2007**, *111*, 1042–1048.
- [94] X. Lin, T. Huang, F. Huang, W. Wang, J. Shi, *J. Mater. Chem.* **2007**, *17*, 2145–2150.
- [95] X. Xiao, C. Liu, R. Hu, X. Zuo, J. Nan, L. Li, L. Wang, *J. Mater. Chem.* **2012**, *22*, 22840–22843.
- [96] Y. Li, J. Wang, H. Yao, L. Dang, Z. Li, *J. Mol. Catal. A Chem.* **2011**, *334*, 116–122.
- [97] K.-L. Zhang, C.-M. Liu, F.-Q. Huang, C. Zheng, W.-D. Wang, *Appl. Catal. B Environ.* **2006**, *68*, 125–129.
- [98] W. Lai Huang, Q. Zhu, *J. Comput. Chem.* **2009**, *30*, 183–190.
- [99] X. Zhang, Z. Ai, F. Jia, L. Zhang, *J. Phys. Chem. C* **2008**, *112*, 747–753.
- [100] J. Henle, P. Simon, A. Frenzel, S. Scholz, S. Kaskel, *Chem. Mater.* **2007**, *19*, 366–373.
- [101] W. Wang, F. Huang, X. Lin, *Scr. Mater.* **2007**, *56*, 669–672.
- [102] S. Zhang, G. Zhang, S. Yu, X. Chen, X. Zhang, *J. Phys. Chem. C* **2009**, *113*, 20029–20035.
- [103] R. Shi, J. Lin, Y. Wang, J. Xu, Y. Zhu, *J. Phys. Chem. C* **2010**, *114*, 6472–6477.
- [104] W.-D. Wang, F.-Q. Huang, C.-M. Liu, X.-P. Lin, J.-L. Shi, *Mater. Sci. Eng. B* **2007**, *139*, 74–80.
- [105] X. P. Lin, F. Q. Huang, W. D. Wang, K. L. Zhang, *Appl. Catal. A Gen.* **2006**, *307*, 257–262.
- [106] W. F. Yao, X. H. Xu, H. Wang, J. T. Zhou, X. N. Yang, Y. Zhang, S. X. Shang, B. B. Huang, *Appl. Catal. B Environ.* **2004**, *52*, 109–116.
- [107] M. Klare, J. Scheen, K. Vogelsang, H. Jacobs, J. A. C. Broekaert, *Chemosphere* **2000**, *41*, 353–362.
- [108] H. Einaga, S. Futamura, T. Ibusuki, *Environ. Sci. Technol.* **2001**, *35*, 1880–1884.
- [109] B. Sun, A. V Vorontsov, P. G. Smirniotis, *Langmuir* **2003**, *19*, 3151–3156.
- [110] T. Sano, N. Negishi, K. Uchino, J. Tanaka, S. Matsuzawa, K. Takeuchi, *J. Photochem. Photobiol. A Chem.* **2003**, *160*, 93–98.

- [111] H. Fujito, H. Kunioku, D. Kato, H. Suzuki, M. Higashi, H. Kageyama, R. Abe, *J. Am. Chem. Soc.* **2016**, *138*, 2082–2085.
- [112] S. Liu, W. Miiller, Y. Liu, M. Avdeev, C. D. Ling, *Chem. Mater.* **2012**, *24*, 3932–3942.
- [113] D. O. Charkin, P. S. Berdonosov, A. M. Moisejev, R. R. Shagiakhmetov, V. A. Dolgikh, P. Lightfoot, *J. Solid State Chem.* **1999**, *147*, 527–535.
- [114] T. J., G. R., V. A., *Phys. status solidi* **1966**, *15*, 627–637.
- [115] J. F. Ackerman, *J. Solid State Chem.* **1986**, *62*, 92–104.
- [116] A. M. Kusainova, S. Y. Stefanovich, V. A. Dolgikh, A. V. Mosunov, C. H. Hervoche, P. Lightfoot, *J. Mater. Chem.* **2001**, *11*, 1141–1145.
- [117] K. Gelderman, L. Lee, S. W. Donne, *J. Chem. Educ.* **2007**, *84*, 685.
- [118] D. L. Postai, C. A. Demarchi, F. Zanatta, D. C. C. Melo, C. A. Rodrigues, *Alexandria Eng. J.* **2016**, *55*, 1713–1723.
- [119] M. Sleiman, P. Conchon, C. Ferronato, J.-M. Chovelon, *Appl. Catal. B-Environmental* **2007**, *71*, 279–290.
- [120] A. Kasahara, K. Nukumizu, G. Hitoki, T. Takata, J. N. Kondo, M. Hara, H. Kobayashi, K. Domen, *J. Phys. Chem. A* **2002**, *106*, 6750–6753.
- [121] N. Buehler, K. Meier, J. F. Reber, *J. Phys. Chem.* **1984**, *88*, 3261–3268.